Accepted Manuscript

Geological Society, London, Special Publications

The Bowland Shale Formation in the Blacon Basin: syngenetic processes, stacking patterns and heat productivity

J. F. Emmings, J. A. I. Hennissen, C. H. Vane, M. Damaschke, L. Marvin, V. Moss-Hayes, A. Lamb, J. Lacey, M. J. Leng & N. J. Riley

DOI: https://doi.org/10.1144/SP534-2022-262

To access the most recent version of this article, please click the DOI URL in the line above. When citing this article please include the above DOI.

Received 29 August 2022
Revised 11 February 2023
Accepted 17 April 2023

© 2023 British Geological Survey, a component body of UKRI. This is an Open Access article distributed under the terms of the Creative Commons Attribution 4.0 License (http://creativecommons.org/licenses/by/4.0/). Published by The Geological Society of London. Publishing disclaimer: www.geolsoc.org.uk/pub_ethics

Supplementary material at https://doi.org/10.6084/m9.figshare.c.6911105

Manuscript version: Accepted Manuscript
This is a PDF of an unedited manuscript that has been accepted for publication. The manuscript will undergo copyediting, typesetting and correction before it is published in its final form. Please note that during the production process errors may be discovered which could affect the content, and all legal disclaimers that apply to the book series pertain.

Although reasonable efforts have been made to obtain all necessary permissions from third parties to include their copyrighted content within this article, their full citation and copyright line may not be present in this Accepted Manuscript version. Before using any content from this article, please refer to the Version of Record once published for full citation and copyright details, as permissions may be required.

The Bowland Shale Formation in the Blacon Basin: syngenetic processes, stacking patterns and heat productivity

Emmings, J. F.[1,2,3], Hennissen, J. A. I.[1], Vane, C. H.[1], Damaschke, M.[1], Marvin, L.[2], Moss-Hayes, V.[1], Lamb, A.[1], Lacey, J. [1], Leng, M. J. [1,4], Riley, N. J.[5]

[1] *British Geological Survey, Keyworth, Nottingham, NG12 5GG, UK*

[2] *School of Geography, Geology and the Environment, University of Leicester, Leicester, LE1 7RH, UK*

[3] *CGG, Tyn Y Coed, Llanrhos, Llandudno, LL30 1SA*

[4] *Centre for Environmental Geochemistry, University of Nottingham, Leicestershire, LE12 5RD, UK*

[5] *Carboniferous Limited, Glendevon, Selby Lane, Keyworth, Nottingham NG12 5AH, UK*

ORCID ID: FA, 0000-0003-2084-0501

*Corresponding author (e-mail: joseph.emmings@cgg.com)

Abstract

We conducted a high-resolution multi-disciplinary analysis of two core sections in the borehole Ellesmere Port-1, Cheshire, UK. Biostratigraphic analysis indicates the core sections are Kinderscoutian and late Arnsbergian-Chokerian in age, respectively. Both cores are assigned to the Bowland Shale Formation (Holywell Shale). Coupled core scan and discrete geochemical analysis enables interpretation of syngenetic processes at a high stratigraphic resolution. Both cores exhibit the classic cyclicity of limestones, calcareous to non-calcareous mudstones and siltstones, interpreted to represent sediment deposition during fourth-order sea level fluctuation. Machine learning of the well log data coupled to the core scan data enabled prediction of the key lithofacies through the entire Bowland Shale interval in Ellesmere Port-1. The machine predictions show the Bowland Shale is interfingered with three turbiditic leaves of the Cefn-y-fedw Sandstone Formation and contains at least 12 complete fourth-order cycles. The Bowland Shale exhibits high radiogenic heat productivity (RHP) in comparison to other sedimentary rocks, due primarily to relative enrichment in U under intermittently euxinic conditions. Thermal modelling, however, shows Bowland Shale RHP contributes a negligible source of additional heat at the scale of 100s m.

Supplementary material: Appendix A contains the discrete bulk geochemical datasets. Appendix B details the calculations used for the heat flow box modelling.

ACCEPTED MANUSCRIPT

Organic and metal-rich mudstones, herein termed black shales, represent an important sedimentary rock type as archives of environmental perturbations (e.g., Wignall, 1994; Algeo, 2004; Kidder and Worsley, 2010; Meyer and Kump, 2008); sources and resources of hydrocarbons (e.g., Tissot and Welte, 1984; Jarvie, 2012a; 2012b), ligands (e.g., Kendrick et al., 2002) and metals (e.g., Gadd et al., 2020); seals for injected CO_2 (e.g., Worden et al., 2020), and; as sources of *in situ* sedimentary heat (e.g., Rybach, 1976; Beardsmore et al., 2011). The UK late Mississippian-early Pennsylvanian Bowland Shale Formation represents a relatively thick black shale succession in the UK (e.g., Waters et al., 2007) with equivalent units in Europe (Kerschke and Schulz, 2013; Zijp et al., 2017), and is a proven unconventional hydrocarbon resource in the UK (Andrews, 2013; Clarke et al., 2018). Here we focus on the Bowland Shale Formation in the Ellesmere Port-1 well, drilled for unconventional hydrocarbons in 2014.

Palpable microseismicity (Clarke et al., 2019), uncertainty related to connectivity to shallow aquifers (e.g., Loveless et al., 2018) and recoverable hydrocarbons (Whitelaw et al., 2019), and overarching net-zero goals (e.g., IPCC, 2014), suggest the Bowland Shale is unlikely to be extensively developed as an unconventional hydrocarbon resource. Despite this, the Bowland Shale Formation remains an important conventional hydrocarbon source rock, for example in the North Sea (Monaghan et al., 2019). The Bowland Shale is a component of at least one geothermal play in the UK where it is a seal for interdigitating sandstone aquifers (Gluyas et al., 2018) and it caps and buries several granitic intrusions in the UK (Busby and Terrington, 2017; Leeder, 1982), potentially enhancing this geothermal play. The Bowland Shale is a candidate source of base metals (Pb-Zn, Cu) (Emmings et al., 2020b; Juerges et al., 2015; Kendrick et al., 2002; Parnell and Swainbank, 1990) and is a borderline highly enriched metalliferous black shale (HEBS) (Emmings et al., 2020c). Weathering of the Bowland Shale may release the redox-sensitive metals and semi-metals into the environment, potentially impacting on groundwater, soil quality and the health of livestock (Brogan et al., 1973; Parnell et al., 2016). The relatively high U content in the Bowland Shale (Emmings et al., 2020c) implicates it as a source of Rn, derived primarily from the decay of ^{238}U, which may contribute to the known Rn hazard in areas such as in the Ribble Valley (Miles et al., 2007) or in deep groundwater aquifers. Finally, the Bowland Shale spans the mid-Carboniferous (Mississippian-Pennsylvanian) boundary and extinction event (Saunders and Ramsbottom, 1986), representing a period of extreme climatic and oceanic conditions of interest to a range of deep time palaeoenvironmental and modern climate research questions (e.g., van de Velde et al., 2021).

Here we integrate sedimentological, geochemical, and petrophysical observations, through two cored sections of the Bowland Shale (historically recognized as the Holywell Shale in North Wales) in Ellesmere Port-1, to develop a high-resolution syngenetic and early diagenetic facies framework through the Bowland Shale. We utilize these observations to build on the idealized sea level faunal/salinity and sedimentary stacking patterns recognized by Ramsbottom et al. (1962) and Holdsworth and Collinson (1988). Using machine learning of wireline data aligned to core scan x-ray fluorescence (XRF) data , we translate core-scale observations into predictions of sedimentological facies through the entirety of the Bowland Shale in Ellesmere Port-1, representing a ca. 324 m thick succession spanning from the Arnbergian (ca. 329 Ma) to the Marsdenian or Yeodonian (ca. 317 Ma). The facies framework and interpreted stacking patterns are relevant for any drilling activity into, or through, the Bowland Shale Formation. Finally, we provide new constraints on the radiogenic heat productivity (RHP) and heat flow through the Bowland Shale in Ellesmere Port-1. In an accompanying

ACCEPTED MANUSCRIPT

paper, Hennissen et al. (this volume) explore the Bowland Shale in Ellesmere Port-1 in the context of hydrocarbon prospectivity.

Geological Setting

Oblique collision between Gondwana and Laurussia during the Carboniferous (Warr, 2000) prompted crustal back-arc extension across central and northern England and North Wales, within a seaway that extended from present-day North America to Poland (e.g., Davies et al., 1999). Extension generated a series of grabens and half-grabens separated by shelves and highs (Fig. 1), termed a 'block-and-basin' topography, aligned along inherited pre-Carboniferous structures and bounded by the Southern Uplands in the north and Wales-Brabant Massif (WBM) in the south (Fraser and Gawthorpe, 1990; Fraser and Gawthorpe, 2003; Leeder, 1982; Waters and Davies, 2006). This array of interconnected basins gradually merged due to post-rift thermal subsidence through the Namurian, and are collectively defined as the Pennine Basin, representing a long-lived depocentre during most of the Carboniferous (Waters and Davies, 2006).

Blacon Basin Structure

Ellesmere Port-1 is situated on the north-east margin of the Blacon Basin in North Wales and Cheshire, a sub-basin of the Pennine Basin (Andrews, 2013) which was possibly linked to the Widnes Basin of Fraser et al. (1990) (Fig. 1). The Blacon Basin is bounded in the south by the Bryneglwys fault (the Bala Lineament) and WBM, in the west by the Nercwys-Nant-figillt Fault Zone (NFZ), Vale of Clwyd Fault and North Wales Shelf, and in the north-east by the Great Ewloe Fault, Edgerley-Waverton Fault Zone (EFZ), and ultimately the Central Lancashire High (Fig. 1) (Smith et al., 2005). The locus of deposition in the Blacon Basin was consistently centred immediately to the north of the Bala Lineament (on the downthrown hangingwall block), as evidenced by; (i) a thick early Carboniferous carbonate succession (Smith et al., 2005); (ii) thickening of Minera Formation (Brigantian) sandstones into the basin (Davies et al., 2004); (iii) early Namurian (Pendleian) megasliding on the south-western fringe of the basin (Kirkham, 2021); (iv) an expanded Namurian succession in the Blacon East-1 well in the Blacon Basin (Andrews, 2013; Davies et al., 2004; Waters et al., 2020); (v) pinch-out of the Namurian succession on the margin of the North Wales Shelf in the west (Williams and Eaton, 1993); (vi) a highly condensed Namurian succession in the Erbistock-1 well on the emergent landmass in the south (Andrews, 2013) (Fig. 1). A condensed Namurian succession is also proven in the Milton Green-1 well (Andrews, 2013) on the nearby Milton Green High (Smith et al., 2005).

During the Brigantian (regional substage in the latest Visean), widespread ramp-to-shelf carbonates of the Clwyd Limestone Group, including the Cefn Mawr Limestone Formation and Minera Formation, indicate development of shallow water carbonate platform and slope conditions (Davies et al., 2004; Davies et al., 2011; Somerville, 1979; Waters et al., 2020). The Cefn Mawr Limestone Formation exhibits shoaling-upwards sequences of wackestone, packestone and crinoidal limestone, often capped by karstic surfaces, soils and calcrete horizons. The sequences were primarily driven by eustatic sea level fluctuation overprinted by late syn-rift tectonism, including subaerial platform exposure during lowstands (Somerville, 1979). The Minera Formation, defined by cyclic sequences of mudstone, packstone, wackestone and calcareous sandstone, represents a fully subaqueous, proximal, sand-rich equivalent to the Cefn Mawr Limestone (Davies et al., 2004). Off platform and

ACCEPTED MANUSCRIPT

distal from detrital sand input, the Brigantian succession grades laterally into the deep-water argillaceous carbonate slope apron facies of the Prestatyn Limestone Formation and the succeeding Teilia Formation (Davies et al., 2011; Warren et al., 1984). Initially shallow waters likely covered the Llŷn-Rossendale Ridge (Jackson et al., 1997; Smith et al., 2005). This high, representing the northern limit to the Blacon Basin, was likely connected to the Central Lancashire High (Fig. 1, *sensu.* Fraser and Gawthorpe, 1990; DECC, 2013) as the manifestation of the south-western end of the Pendle fault system (Pharaoh et al., 2019a). The presence of the Prestatyn Limestone and Teilia Formation near the north-east margin the North Wales Shelf suggests the Llŷn-Rossendale Ridge was a discontinuous feature, enabling weak connectivity between the Blacon Basin and distal Craven Basin (Andrews, 2013; Davies et al., 2004; Juerges et al., 2015; Waters et al., 2007).

A transition from Clwyd Limestone Group to the Craven Group at the Visean-Namurian boundary indicates an important regional shift from active rifting to thermal subsidence (Leeder, 1982; Waters et al., 2009), and as a consequence, a switch from carbonate to siliciclastic depositional system (e.g., Fraser et al., 2003). Cessation of active rifting and onset of thermal subsidence prompted progressive infill of the inherited Visean basin structures during the Namurian (Fig. 1). Assuming relatively sheltered conditions (Peters and Loss, 2012) the inherited platforms and highs likely initially exhibited a water depth of less than 50 m. Taking the proximal Craven Basin as an analogue (Emmings et al., 2020a), water depth in the Blacon Basin likely ranged from ~100 to 200 m on the flanks and highs (Davies, 2008; Holdsworth and Collinson, 1988) to several hundred metres in the deepest part of the basin (Davies et al., 1993).

Namurian Stratigraphy

The Pentre Chert Formation represents the basal part of the Craven Group in the Blacon Basin (Fig. 2), which unconformably overlies the Clwyd Limestone Group (Davies et al., 2004). The Pentre Chert is defined as a sponge spicule- and radiolarian-bearing chert deposited in relatively deep water, below storm wave base (Davies et al., 2011). The Pentre Chert likely represents the condensed counterpart of Pendleian (E_1) siliceous mudstones of the Bowland Shale Formation in the Craven Basin (Emmings et al., 2020a; Emmings et al., 2020b). During the Pendleian, most of the siliciclastic sediment was sourced from the Pendle delta system in the north of the Craven Basin (Fraser and Gawthorpe, 1990; Fraser and Gawthorpe, 2003; Waters and Condon, 2012), ensuring the Blacon Basin remained isolated from detrital sediment. Deposition of siliceous sediments in the Blacon Basin during the Pendleian is consistent with; (i) development of widely hypoxic or intermittently anoxic bottom water conditions, favoring colonization by sponges (e.g., Schuster et al., 2021); (ii) water column conditions which favoured colonization by radiolarians (Emmings et al., 2020a; Emmings et al., 2020c), perhaps associated with elevated riverine nutrient-loading and/or silica input (Dunham and Wilson, 1985), and; (iii) increased influx of detrital mud onto platforms (potentially a distal extension of the Pendle delta), prompting regional termination of carbonate production (Davies et al., 2004).

The Pentre Chert is overlain by the Bowland Shale Formation (herein Bowland Shale), a highly heterogeneous, mudstone-dominated succession, spanning from the mid-late Pendleian (ca. 329 Ma) to Marsdenian or Yeodonian in Ellesmere Port-1 (ca. 317 Ma; Fig. 2) (Davies et al., 2011; Waters and Condon, 2012). The Bowland Shale definition adopted (Waters et al., 2009) encompasses the Holywell Shale in North Wales (e.g., Davies et al., 2004; Newport et al., 2016). The onset of third to

ACCEPTED MANUSCRIPT

fourth-order sea level fluctuation (Mitchum and Van Wagoner, 1991; Waters and Condon, 2012) coupled to thermal subsidence prompted deposition of the Bowland Shale across a wide range of basinal, prodelta, and periodically emergent shelfal environments (Davies et al., 2004). The Pentre Chert and Bowland Shale grade laterally southwards into the Cefn-y-fedw Sandstone Formation of the Millstone Grit Group derived primarily from the WBM (Fig. 2) (Davies et al., 2004; Waters et al., 2009; Waters et al., 2020). The Cefn-y-fedw Sandstone comprises coarsening-upward cycles of quartzitic sandstones interbedded with subordinate mudstone and coal beds, interpreted as fluviodeltaic progradational sequences (Davies et al., 2004; Waters et al., 2020). In the Blacon Basin, three turbidite sand packages within the Bowland Shale represent the distal extensions of the Lower, Middle and Upper Cefn-y-fedw Sandstone units (Davies et al., 2004; Waters et al., 2020). The Cefn-y-fedw Sandstone is analogous and equivalent to sands of the Morridge Formation in the Widmerpool Gulf and Edale Gulf (Hennissen et al., 2017; Morton et al., 2015; Waters et al., 2009); both are associated with delta systems shed from the WBM in the south (Fraser and Gawthorpe, 1990; Waters et al., 2020). The Bowland Shale grades into, and is overlain by, the fluviodeltaic Gwespyr Sandstone Formation (also Millstone Grit Group). Waters et al. (2020) showed the Gwespyr Sandstone Formation derives from a complex mixture of provenances from the south, north and west.

Marine bands. Marine transgressions and associated maximum flooding surfaces in the Bowland Shale are manifested as carbonate-rich, typically macrofauna-bearing sedimentary packages termed 'marine bands' (e.g., Ramsbottom, 1977). Sea level cyclicity in the Namurian was likely driven by far-field glaciation on Gondwana (Veevers and Powell, 1987). The amplitude of sea level fluctuation is estimated at 42 m (Maynard and Leeder, 1992) or 60-100 m (Church and Gawthorpe, 1994; Rygel et al., 2008). Marine bands on shelves mark the base of cyclothemic 'Yoredale' limestone-shale-sandstone triplets commonly capped by coal (e.g., Hampson et al., 1997; Davies et al., 2004; Waters et al. 2007; Dean et al., 2011). Basinal marine bands are typically 1-5 m thick and often overlain by an asymmetrical sequence of; (i) non-bioclastic, hemipelagic (lenticular) mudstone, and; (ii) turbidites, hybrid beds and debrites (Emmings et al., 2020a; Martinsen et al., 1995). Lowstands were associated with localised to extensive basinal sand deposition depending on proximity to delta systems (Millstone Grit Group). The third and fourth-order marine band cycles are possibly superimposed onto 1.1-1.35 Myr duration Namurian 'mesothem' cycles (Ramsbottom, 1979), associated with 17 major base-level falls (Waters and Condon, 2012) and shifts in the loci of sediment deposition (Martinsen et al., 1995). Salinity fluctuations from fully marine (transgressions) to brackish or freshwater conditions are also widely recognized in the Bowland Shale, on the basis of volumetric calculations (Holdsworth and Collinson, 1988), macrofauna and microfauna such as conodonts (Holdsworth and Collinson, 1988; Ramsbottom et al., 1962), biomarkers (Sims et al., this volume) (Gross et al., 2015), sedimentology (Emmings et al., 2020a; Emmings et al., 2020c; Gross et al., 2015; Holdsworth and Collinson, 1988) and inorganic geochemistry (Emmings et al., 2020c; Leeder et al., 1990; Maynard et al., 1991).

Coupled to sea level and salinity fluctuation, palaeoredox proxies show the Bowland Shale was deposited under fluctuating oxic, anoxic and at least intermittently sulphidic (euxinic) conditions (Emmings et al., 2019; Emmings et al., 2020c; Gross et al., 2015; Leeder et al., 1990; Riley et al., 2016), a phenomenon likely driven by euhaline phytoplankton productivity. Euxinia in the Bowland Shale (and younger Carboniferous rocks) is most strongly associated with transgressions and maximum flooding, whereas reduced basin accommodation is linked to increased bottom water

ACCEPTED MANUSCRIPT

ventilation (Bloxam and Thomas, 1968; Emmings et al., 2020c; Fisher and Wignall, 2001; Gross et al., 2015; Leeder et al., 1990; Maynard et al., 1991; Pearce et al., 2010). Considering the evidence for significant freshwater discharge from delta systems, *shelfal* anoxia was possibly caused by upwelling of marine anoxic bottom waters trapped beneath a freshwater lid (Algeo et al., 2008). By contrast trace element quotas in the *basinal* shales favour development of anoxia in weakly restricted, thermally stratified and highly productive water column conditions (Emmings et al., 2020c; Riley et al., 2016). Euxinia was potentially confined to mid-depth waters, potentially part of one or more linked regional-scale oxygen minimum zones (OMZs) which developed in the late Devonian (Emmings et al., 2022; Kabanov and Jiang, 2020).

Macrofauna associated with the marine bands form the basis of a high-resolution biostratigraphic framework through the Namurian (Holdsworth and Collinson, 1988; Ramsbottom and Saunders, 1985). Marine bands and overlying mudstones exhibit the following idealized faunal sequence (phases 6 to 1); thick shelled ammonoids (6), thin shelled ammonoids (5), molluscan spat (4), lingula (3), planolites (2), fish remains (1) and barren zones (Baines, 1977; Ramsbottom et al., 1962; Ramsbottom, 1977). These faunal phases are thought to indicate cycling between euhaline (6) and freshwater conditions (1) (Holdsworth and Collinson, 1988; Ramsbottom et al., 1962), although preservation or absence of bioclasts is also dependent on early diagenetic porewater conditions (Emmings et al., 2020c). The Bowland Shale in North Wales spans all the regional Namurian substages, from the Pendleian (E_1) to Yeodonian (G_1) (Davies et al., 2011). Marine bands exhibit an average periodicity of 111 ka (Waters and Condon, 2012), indicative of fourth-order cycles (Mitchum and Van Wagoner, 1991). $E_{1c}1$, $E_{2a}2$, $E_{2b}3$, H_{1a}, H_{2b1}, R_{1b}, $R_{1c}4$, $R_{2a}1$, $R_{2b}1$, $R_{2c}1$, $G_{1a}1$ and $G_{1b}1$ peak flooding events are recognized in North Wales (Davies et al., 2011), likely related to third-order forcing (Mitchum and Van Wagoner, 1991; Waters and Condon, 2012). Multiple flooding surfaces are recognised for many of the marine bands, potentially linked to sub-100 ka precession or obliquity cycles (Waters and Condon, 2012).

Burial and Uplift

Pb-Zn mineralization on the North Wales Shelf suggests thermal maturation and dewatering of adjacent basinal sediments in the latest Namurian (Juerges et al., 2015). During the late Pennsylvanian, closure of the Rheic-palaeo-Tethys seaway associated with the Variscan Orogeny (e.g., Leeder, 1982) prompted a major depositional hiatus and the inversion of many basin structures across central England (e.g., Smith et al., 2005). In the Pennines, inversion combined with a relatively high basinal heat flow (in contrast to North Wales) enhanced basin dewatering and led to protracted Pb-Zn-F mineralization on blocks (Bouch et al., 2006; Hollis and Walkden, 2012). Inverted structures in the vicinity of the Blacon Basin include the anticlines on the Bala Lineament and EFZ (Smith et al., 2005) and the Môn-Deemster-Ribblesdale fold belt in the north (Arthurton, 1984; Pharaoh et al., 2019a). The Cheshire Basin, partially superposed on the Blacon Basin, developed in response to renewed extension during the Permo-Triassic (Davies et al., 2004). The Permo-Triassic in the Cheshire Basin comprises aeolian and fluvial sediments (Sherwood Sandstone Group); Fe-Cu mineralization on the adjacent North Wales Platform may derive from charging by Permo-Triassic oxidized brines (Juerges et al., 2015) or from basinal Carboniferous fluids (Parnell and Swainbank, 1990). Maximum burial of the Blacon Basin was likely attained in the Late Cretaceous, prior to Tertiary uplift (Green et al., 1997; Pharaoh et al., 2019b; Williams and Eaton, 1993).

ACCEPTED MANUSCRIPT

Materials and Methods

Logging and sampling

Two 17.8 m cored sections through the borehole Ellesmere Port-1 (53°17'43.3841", 02°54'21.13091"; 339629 mE 378016 mN, British National Grid), drilled by IGas Energy in 2014, were logged and sampled at the National Geoscience Data Centre (NGDC) core repository, British Geological Survey. Sedimentological structures and facies were logged prior to major and minor element XRF core scanning and sampling. The reported absolute core depths were aligned to the reported wireline absolute depth by matching features observed in core to the borehole image logs (Figs. 2-3). For validation, we compared synthetic (derived from discrete XRF) and measured gamma-ray curves (Fig. 2). The wireline gamma ray tends to smooth across thin beds exhibiting particularly high or low true (synthetic) gamma ray values, but overall, the synthetic and wireline gamma ray datasets are strongly correlated (Fig. 2d). This assessment indicated an offset of 1.6 and 1.76 m between the downhole absolute depth and reported cored depth, for core 1 and core 2, respectively. Synthetic total gamma ray was estimated from bulk U, Th and K concentrations using the approximation of Ellis and Singer (2007) (Eq. 1).

$$GR\ (API) = 4Th+8U+16K \quad (1)$$

Core scan X-ray fluorescence (XRF) measurements were collected using an Itrax MC core scanner (Cox Analytical Systems) in the Core Scanning Facility (CSF) at the British Geological Survey, Keyworth. This dataset is available under Open Government License (BGS Core Scanning Facility, 2022). Before core scanning, fragments of the split core were aligned with a levelling tool to ensure optimal alignment of the detector. XRF was measured at a 1 cm step-size and 30 s integration time. For each core section, an initial surface scan was performed to compute the trajectory of the XRF detector. The Itrax MC core scanner automatically produces an XRF sum spectrum for each core section, which was peak-fitted using the processing software Q-Spec version 8.6. A single fitting template was used to fit most of the core data. Core horizons that showed high Ca, Fe or Cl elemental abundances were refitted accordingly. These fitted XRF data were exported as elemental peak areas (counts) for processing in R. Data were aggregated into the two core runs and assigned a true core depth. The dataset was cleaned to remove erroneous data points, for example spanning cracks, missing core sections and intervals of generally poor core quality.

Bulk Geochemistry

A total of 110 samples, split between core 1 (57 samples) and core 2 (53 samples), were selected for bulk major and trace element geochemistry, RockEval pyrolysis, palynology (see Hennissen et al. this volume) and stable isotope analysis. Discrete XRF major and trace element data were acquired on fused beads (using ignited sample powders) and powder briquettes at the University of Leicester, using a PANalytical Axios Advanced XRF spectrometer and default PANalytical SuperQ conditions (Malvern PANalytical, Malvern, UK). Repeat analyses of reference materials and prior Bowland shale samples indicates an XRF accuracy of ± 5 % for major elements and ± 5 % for trace elements, and precision up to ± 5 % (but commonly ± 1 %, 2σ) for major elements and ± 10 % (but commonly ± 5 %) for trace elements (Emmings, 2018; Emmings et al., 2020c).

ACCEPTED MANUSCRIPT

Total sulphur (TS) content was determined via a Flash 1112 elemental analyser coupled to an isotope ratio mass spectrometer at the National Environmental Isotope Facility (NEIF) laboratory at the British Geological Survey. TS accuracy and precision is estimated at ± 15 % and ± 0.2 wt. % S, respectively, based on repeat analyses and independent measurement via LECO elemental analysis (Emmings et al., 2020c). Trace element enrichment factors (EFs; e.g., Tribovillard et al., 2006) were utilised using Post-Archaean Average Shale (PAAS) (Taylor and McLennan, 1985) (Eq. 1) and local mean concentrations (*sensu.* Emmings et al., 2020c). Pyrolysis was conducted in standard mode using a Rock-Eval 6^{TM} apparatus (Vinci Technologies, Nanterre, France) at the British Geological Survey. Accuracy is typically 1-2% for most Rock-Eval parameters, based on repeat analyses of the IFP Rock-Eval standard. Repeat analyses of similar Bowland shale samples indicates precision (2σ) of ± 0.11 mgHC/g (S1), ± 0.44 mgHC/g (S2) and ± 0.03 wt. % total organic and inorganic carbon (TOC, MINC). Derived RockEval parameters include oil saturation index (OSI) and hydrogen index (HI) (Lafargue et al., 1998).

$$EF_{element}=(X/Al)_{sample}/(X/Al)_{PAAS} \quad (2)$$

Original TOC (TOC_o) was calculated for palynological samples using the method of Jarvie (2012a) and are reported in Hennissen et al. (this volume). TOC_o was extrapolated for all discrete samples (n = 110) via a linear regression between the calculated TOC_o and present-day TOC (TOC_{pd}, r^2 = 0.99, see appendix, Eq. 3), where;

$$TOC_o = 1.16TOC_{pd} - 0.16 \quad (3)$$

On the basis that the core sections are oil to marginally gas-mature (Hennissen et al., this volume), TOC_o was preferred over TOC_{pd} for a more robust S/TOC palaeosalinity proxy (Raiswell and Berner, 1987).

Stable Isotopes. All stable isotope data are reported in standard delta (δ) notation as per mille (‰) variations. Bulk S isotope ratios were measured using a Thermo Fisher Delta Plus XL isotope ratio mass spectrometer interfaced with a Flash 1112 elemental analyser. $\delta^{34}S_{bulk}$ values are reported on the VCDT scale. S isotope ratios were calibrated using a linear fit through IAEA-S-1 (−0.3‰), IAEA-S-2 (+22.67‰) and IAEA-S-3 (−32.3‰). $\delta^{34}S_{bulk}$ reproducibility is ±1.2‰ (2σ) based on repeat analyses.

Bulk C isotope analyses were performed by combustion in a Costech ECS4010 Elemental Analyser (EA) on-line to a VG TripleTrap and Optima dual-inlet mass spectrometer, with $\delta^{13}C$ values calculated to the VPDB scale using a within-run laboratory standards calibrated against NBS-19 and NBS-22 (VPDB) scale, using within-run laboratory standards (NBS19 +1.95‰ and NBS22 −30.03‰). $\delta^{13}C_{org}$ reproducibility is $\pm$ <0.1‰ (1 SD). C/N ratios are calibrated against a Broccoli standard (BROC2). Replicate analysis of well-mixed samples indicated a precision of $\pm$ <0.1.

Data manipulation and analysis

All data manipulation and statistical analysis was coded in R using RStudio (R Core Team, 2018). XRF core scan, discrete analyses (conventional XRF, stable isotopes, RockEval pyrolysis) and wireline data were manipulated using the following R packages; *ggplot2* (Wickham, 2009), *gridExtra* (Auguie, 2016), *zoo* (Zeileis and Grothendieck, 2005), *plyr and dplyr* (Wickham and Francois, 2016), *data.table*

ACCEPTED MANUSCRIPT

(Dowle and Srinivasan, 2020), *compositions* (van den Boogaart et al., 2020), *ggtern* (Hamilton, 2017), and *caret* (Kuhn, 2020). *Chemofacies* were determined by hierarchical cluster analysis (HCA) of principal component analysis (PCA) scores (e.g., Emmings et al., 2022) using selected core scan XRF major and minor elements (Mg, Al, Si, P, K, Ca, V, Mn, Fe, Ni, As, Sr, Zr, Mo and Ba). These elements were selected on the basis of relatively high abundances, and as proxies for detrital phases (Al, Si, K, Zr; e.g., Emmings et al., 2020a, Hild and Brumsack, 1998), Fe-oxides (Fe, As; e.g., Tribovillard et al., 2020), autochthonous input including biogenic and diagenetic carbonates (Si, Ca, Mn, Mg, Sr, Ba, P) and palaeoredox (Fe, Mn, Mo, V, Ni, As; e.g., Tribovillard et al., 2006). Processed count data were not converted to absolute concentrations; this approach circumvents closed data effects which require transformation prior to statistical analysis (e.g., centred log-ratio; Aitchison, 1986). PCA was conducted on the correlation matrix (scaled and centred data). The first six principal components were selected on the basis of assessment of the hinge point on the scree plot. HCA of the sample scores for the first six principal components was conducted via the sum of squares (Ward clustering) and Euclidian distance matrix.

Machine learning. We explored the potential of machine learning to aid extrapolating the core scan clusters (e.g., chemofacies) through the Bowland Shale Formation. Ahead of machine learning, the seven chemofacies were aggregated into four classes; limestones (A), weakly to moderately calcareous mudstones and siltstones (C-E), claystone density flow deposits (B, F) and siltstone to sandstone density flow deposits (G). Simplification into four classes for machine learning was justified on the basis of (1) experimentation in order to optimize the balance between the accuracy and complexity of predictions, and; (2) the thickness of beds and co-occurrences with other chemofacies – specifically, laminae of siderite-cemented claystone or siltstone are not directly resolvable in the well log data, but commonly co-occur with the claystone chemofacies (F).

The k-nearest neighbour (kNN) algorithm was selected for machine learning based on superior accuracy compared to linear discriminant analysis (LDA), classification and regression trees (CART), Support Vector Machine (SVM) and Random Forest methods. The four simplified chemofacies classes were matched to the nearest, depth-aligned well log datum. The models were trained and deployed using the following well log data; compensated neutron porosity (CN), compressional wave slowness (DTC), shear wave slowness (DTS), spectral gamma (U, Th, K), photo-electric (PE) and calculated formation bulk density (ZDEN). We trialed three approaches; (1) kNN using raw wireline data (87% accuracy at 0.05 p-value, optimal k = 7); (2) kNN using standardized (scaled and centred z-score) wireline data (89% accuracy at 0.05 p-value, optimal k = 5); (3) kNN using standardized data and with null well log values (-9999) removed (87% accuracy at 0.05 p-value, optimal k = 5). Training, verification, and accuracy estimation was determined on a 4:1 training-to-verification split. It is beyond the scope of this chapter to further refine the machine learning algorithms, but future work could impute null values (e.g., Dmitrijeva et al., 2020) as a compromise between methods (2) and (3). The trained models were deployed on the entire Bowland Shale section at Ellesmere Port-1 (1443 to 1767 m below surface) to delineate limestone, calcareous mudstone, claystone, and siltstone to sandstone (density flow).

Radiogenic heat productivity and heat flow

Radiogenic heat productivity (RHP, $\mu W/m^3$) was calculated using the equation of Rybach (1976) (Eq. 4);

ACCEPTED MANUSCRIPT

$$RHP = (1000p)(10^{-5})[(9.52U)+(2.56Th)+(3.48K)] \quad (4)$$

Where U, Th and K concentrations are in ppm, ppm and wt. %, respectively, and p is the bulk density (g/cm^3). We assume p = 2.6 g/cm^3 for the Bowland Shale (Clarke et al., 2018). The temperature gradient through the Bowland Shale was modelled using the equation of Beardsmore et al. (2010), where T is the temperature at the base of the given sedimentary package, T_0 is the temperature at the top of the package, Q_0 is the surface heat flow (W/m^2), K_s is the thermal conductivity (W/mK), A_s is RHP (in W/m^3) and S is the thickness of the sedimentary package (m), and inversely proportional to the thermal conductivity (K_s in W/mK), as defined by (Eq. 5);

$$T\,[°C] = T_0 + [(Q_0 \times S)/K_s] - (A_s)[S^2/(2K_s)] \quad (5)$$

Results and Discussion

Syngenetic processes

Based on macrofaunal (ammonoid) biostratigraphy, cores 1 and 2 are assigned to the Late Kinderscoutian (R_1c1) and late Arnsbergian-Chokerian (H_{1a}1-H_{1a}3) biozones, respectively (Figs. 4-5). Thus, core 2 spans the onset of the Mid-Carboniferous boundary (Saunders and Ramsbottom, 1986), although the presence of intervening faults and a paucity of diagnostic Ansbergian macrofauna does not preclude the potential for hiatuses beneath the H_{1a}1-H_{1a}3 interval. The core sections comprise packages of; (1) massive, weakly to strongly calcareous, non-bioclastic to bioclastic mudstones, often interbedded with thin limestone beds, overlain by; (2) thinly laminated or chaotic, non-calcareous claystone beds (Figs. 4-5). The calcareous, bioclastic mudstones are often macrofauna-bearing and are collectively interpreted as basinal marine band facies, characteristic of the Bowland Shale, deposited during fourth-order marine transgressions and highstands (e.g., Martinsen et al., 1995, Waters and Condon, 2012).

The overlying non-calcareous claystone packages represent deposition from a range of turbulent, hybrid and laminar flows (e.g., Talling et al., 2012) during falling basin accommodation (Figs. 4-5). In some cases the non-calcareous claystone packages contain pyritized organic matter and pyrite nodules, similar to the Bowland Shale in the Craven Basin, suggestive of intermittently non-steady state sulphidic pore water conditions (Emmings et al., 2020c). In many cases, consecutive, stacked chaotica suggests the claystone packages were transported en masse, potentially as discrete, metre-scale blocks rafted within debris flows (e.g., mass transport deposits; MTDs). Towards to the top of both core sections, the non-calcareous claystones are capped by thinly to thickly laminated, interbedded, bioturbated siltstone and sandstone facies, likely deposited during lowstands. In core 1, the contact between the siltstones and the underlying claystones is faulted; thus, the sequence stratigraphic relationship is unclear.

Zr/Al aliases the heavy mineral (zircon) component and is interpreted as a local proxy for the detrital grain size in this system (e.g., silt- to sand-fraction; Dowey and Taylor, 2019, Emmings et al., 2020a). This is consistent with the observed relationship between Zr/Al and sedimentary facies; the marine band, claystone and siltstone facies exhibit low, medium, and high to very high Zr/Al, respectively (Figs. 4-5). Mo is a redox-sensitive metal that is fixed under at least intermittently sulphidic pore

ACCEPTED MANUSCRIPT

water conditions (e.g., Tribovillard et al., 2006). Elevated Mo/Al within the marine band packages (in both core sections) suggests development of anoxic and intermittently sulphidic conditions coupled to sea level rise. This is consistent with a productivity-driven, weakly restricted model for anoxia during deposition of the Bowland Shale (Emmings et al., 2020c). As is also redox-sensitive in the marine environment, but interpretation in terms of palaeoredox is generally complex (Tribovillard, 2020). In this system, As/Al tends to co-vary with Mo/Al (Figs. 4-5); this suggests operation of a strong Fe-Mn (oxyhydr)oxide shuttle during deposition (Tribovillard, 2020), analogous to the model for anoxia in the adjacent Craven Basin (Emmings et al., 2020c). As/Al enrichment tends to span a wider depth interval compared to Mo/Al, and As/Al sinuosity, particularly in core 1, suggests generally high sensitivity to intermediate redox conditions compared to Mo/Al. Thus, high As/Al coupled to low Mo/Al is interpreted to indicate ferruginous water column conditions overlying non-sulphidic pore waters (Figs. 4-5).

Finally, the palaeosalinity measure Sr/Ba (Wei and Algeo, 2019) shows conditions were generally marine and intermittently brackish. Whilst the Sr/Ba salinity proxy is limited to non-carbonate-bearing lithologies, the presence of euhaline macrofauna within the marine band facies permits a comprehensive reconstruction of the palaeosalinity variation throughout both cores (Figs. 4-5). Several of the interpreted falling stage to lowstand sedimentary packages exhibit Sr/Ba < 0.5; this suggests deposition under at least intermittently brackish conditions during periods of reduced basin accommodation. Sr/Ba shows reduced salinity was more prevalent in the Late Kinderscoutian section (core 1) compared to the generally more saline Arnsbergian-Chokerian section (core 2); this is consistent with the increasing proximity (i.e., progradation) of the Cefyn-y-fedw delta system towards the top of the Bowland Shale.

Cluster analysis of selected XRF core scan major and minor elements delineates seven chemofacies (A-G), interpreted as; limestone deposited under sulphidic conditions (A), siderite-cemented claystone or siltstone deposited under mixed redox conditions (B), bioclastic, moderately to strongly calcareous mudstone deposited under sulphidic conditions (C), weakly to moderately calcareous phosphatic mudstone deposited under mixed redox conditions (D), weakly bioclastic, weakly calcareous mudstone deposited under weakly sulphidic to non-sulphidic conditions (E), claystone deposited under oxic or suboxic conditions (density flows) (F) and siltstone to sandstone deposited under oxic or suboxic conditions (density flows) (G). Thus, the chemofacies are an objective measure for lithological variation, supplementary to the conventional sedimentological descriptions (Figs. 4-5). The XRF core scan chemofacies are generally consistent with the conventional sedimentary descriptions, although there are some discrepancies, particularly in the assignment of calcareous and non-calcareous sediments. This is best explained by the difficulty in the visual estimation of the fraction carbonate (e.g., reaction with a small amount of HCl).

A pseudo-compositional ternary plot of the core scan XRF data indicates most intervals are argillaceous, and less commonly quartz or carbonate-rich (Fig. 6). Carbonate-bearing, siliceous mudstones are rare (Fig. 6); this is consistent with the absence of silica cementation in the two cored sections. The discrete quantitative XRF analyses support this observation; dual Si versus Al (Fig. 7a), and Si versus Zr (Fig. 7b) biplots of Emmings et al. (2020b) shows biogenic silica is negligible in the two cored intervals. Thus, it is clear the cored sections are not comparable to, or transitional from, the underlying Pentre Chert, and do not contain reworked biogenic silica. By extension, the lack of pervasive cementation shows the cored sections in Ellesmere Port-1 are not comparable to key

ACCEPTED MANUSCRIPT

intervals in the Craven Basin, such as; (1) the siliceous mudstones of the Upper Bowland Shale (Emmings et al., 2020b), and; (2) the calcareous and siliceous mudstones and limestones of the Lower Bowland Shale (e.g., Fauchille et al., 2017; Fauchille et al., 2018; Newport et al., 2018). Instead, the observed pattern of interfingering argillaceous and carbonate marine band facies is more comparable to the Bowland Shale in other paralic basins, such as the Widmerpool Gulf (Hennissen et al., 2017; Könitzer et al., 2014).

Each discrete sample spans ca. 2 cm stratigraphic thickness. Taking a local mean sediment accumulation rate (mSAR) of ca. 22 mm/kyr (Emmings et al., 2020b, after Davies et al., 2004) and 55% compaction (Emmings et al., 2020a), each sample represents ca. 2 kyr duration. This is a first-order estimate since the compaction ratio and mSAR is dependent on sedimentary facies (e.g., Shanmugam and Moiola, 1982; Droxler and Schlager, 1985; Emmings et al., 2020a). Enrichment factors for discrete XRF analyses support the interpretations based on the core scan XRF dataset. The strongly to weakly carbonate-bearing chemofacies (A-E) are consistently enriched in a suite of redox-sensitive elements, including Se, Mo, U, Zn, V, Ni and Fe (Fig. 8). Se enrichment is a prominent and unusual characteristic of the Bowland Shale that is best explained by ashfall inputs from far-field active volcanic centres (e.g., Brandon et al., 1995; Spears et al., 1999) or derived from weathering of volcanic rocks in the hinterland, followed by trapping under sulphidic conditions (Parnell et al., 2016). Parnell et al (this volume) show Se, Mo and to a lesser degree As, are complexed with organic matter and contained within pyrite in the Bowland Shale. By contrast Cu and U, other important redox-sensitive elements, are primarily hosted within recalcitrant (e.g., silicate or refractory kerogen) phases.

Chemofacies A limestones are fine grained, lack bioclasts and exhibit high concentrations of elements which proxy for carbonate, including Ca, Mg and Ba (Fig. 8). The limestone beds also lack internal sedimentary structures, suggestive of an early diagenetic origin (e.g., spherulitic limestones; Emmings et al., 2020c). Enrichment in redox-sensitive elements suggests early diagenetic precipitation via anaerobic oxidation of methane (Mazzini et al., 2004), similar to Pendleian spherulitic limestones observed in the Craven Basin (Emmings et al., 2020a). Siderite-cemented beds (chemofacies B) are most commonly interbedded with the claystone facies and exhibit relatively high concentrations of Mg, Fe and Mn, and moderate Ca (Fig. 8), consistent with dolomite and/or siderite cementation. The marine band packages are dominated by bioclastic calcareous mudstones (chemofacies C and D), interpreted as hemipelagic muds interbedded with subordinate calci-turbidites. The phosphatic chemofacies D is rare in core 1 and more common in core 2, consistent with phosphate input or fixation associated with generally more marine and productive conditions during the Arnsbergian (e.g., fish debris, authigenic phosphate). The marine band packages are typically overlain by chemofacies E, F and/or G, interpreted as falling sea level and/or lowstand deposits.

The low $\delta^{34}S_{bulk}$ and large offset from $\delta^{34}S$ of contemporaneous seawater sulphate of ca. 13-15 ‰ (Kampschulte et al., 2001; Kampschulte and Strauss, 2004) in chemofacies A-E suggests precipitation of solid sulphides under open system conditions (e.g., Mossmann et al. 1991). In contrast, chemofacies F and G lack enrichment in redox-sensitive elements and exhibit variable, relatively high $\delta^{34}S_{bulk}$ (Fig. 8). High $\delta^{34}S_{bulk}$ in chemofacies F and G is best explained by precipitation of pyrite under closed system (i.e., relatively late diagenetic) conditions and/or quantitative sulphate. Any sulphate in chemofacies F and G is likely to be finely disseminated in the sedimentary matrix. Leached zones

ACCEPTED MANUSCRIPT

along margins of the conjugate faults at ca. 1537.73 in core 1 (Fig. 5) exhibit $\delta^{34}S_{bulk}$ of +19.8 to +22.6 ‰; this is best explained by presence of secondary sulphate that precipitated during the passage of late diagenetic oxidizing fluids.

Mississippian terrestrial OM typically exhibits −23.9‰ (Peters-Kottig et al., 2006) to −25.1‰ $\delta^{13}C_{org}$ (Könitzer et al., 2016), whereas amorphous organic matter (AOM; of probable marine origin) is usually close to ca. −29.1‰ (Lewan, 1986). $\delta^{13}C_{org}$ exhibits a consistent range between –27‰ and –24‰ in all sedimentary facies (Fig. 8), favouring a generally mixed to terrestrial origin to the organic matter (see Hennissen et al., this volume, for further discussion). The C/N ratio is relatively wide ranging (C/N 5-25). The marine, hemipelagic, anoxic chemofacies (A-D) have higher C/N than the oxic, density flow chemofacies (F-G). Considering C/N as a proxy for organic matter type, the C/N ratios are counter-intuitive because cellulose, abundant in C3 and C4 land plants, is N-deficient. Thus, fresh land plant material typically has C/N > 20 whereas marine algal and bacterial sources has C/N < 10 (Meyers, 1994). Yet the reverse is observed in the two core sections; chemofacies F-G, comprising abundant Type III terrestrial organic matter (Hennissen et al., this volume), have relatively low C/N, whereas the marine facies have high C/N (Fig. 8). This discrepancy shows C/N is a poor measure for organic matter type in these rocks (consistent with e.g., Mercuzot et al., 2021 and references therein). Low C/N in argillaceous sediments (chemofacies F-G) is best explained by a quantitative contribution from inorganic (clay-bound) NH_4^+ (Lindgreen, 1994), whereas high C/N in the anoxic facies is consistent with the preferential degradation of nitrogen-rich amino acids under suboxic conditions (Van Mooy et al., 2002).

Finally, dual assessment of S/TOC_o and Sr/Ba palaeosalinity proxies (Berner and Raiswell, 1984; Wei and Algeo, 2019), Mo versus U enrichment factors (Algeo and Tribovillard, 2009; Tribovillard et al., 2012) and Mo versus TOC_o (Algeo and Lyons, 2006) (Fig. 9a-c) provide further support for a weakly restricted, productivity-driven model for anoxia (Fig. 9d-g). Two samples exhibit $S/TOC_o < 0.1$ at 1533.00 and 1536.36 m in core 1 (Fig. 5, 9a), which suggests development of at least intermittently fully fresh bottom water conditions. The results of palynological analysis (Hennissen et al., this volume) supports the sequence stratigraphic framework and model for anoxia. Marine transgressions often show a step change from (1) proximal or marginal, (sub)oxic shelf edge palynofacies in the underlying lowstand packages into (2) anoxic shelf to basin palynofacies in each marine band package (Figs. 4-5). The bioturbation analysis of Hennissen et al. (this volume) is also consistent with the interpreted palaeoredox cyclicity.

Overall, the sedimentological observations, patterns of redox-sensitive metals and semi-metals both in core scan (Figs. 4-5) and discrete (Fig. 8) samples, S and C stable isotopes, C/N and palynology (Fig. 8, Hennissen et al., this volume) support a model of productivity-driven marine anoxia (Emmings et al., 2020c). Anoxia was likely driven by productive marine phytoplankton and the export of highly labile organic matter into bottom waters, in a weakly restricted basin (Emmings et al., 2020c). Falling sea level induced progradation of a freshwater lid into the Blacon Basin; a process that led to the shut-down in photic zone marine productivity and consequent basin ventilation, whilst generally sustaining normal marine or moderate salinities in bottom waters. Thus, the palaeosalinity record often lags the palaeoredox signal (Fig. 9). Based on S/TOC_o, bottom waters were fully desalinated only once, during a well-developed lowstand in the upper part of the Kinderscoutian section (core 1) (Fig. 5).

ACCEPTED MANUSCRIPT

Stacking patterns and basin fill

Three k-nearest neighbour (kNN) machine learning algorithms were deployed to predict siltstone and sandstone (chemofacies G), claystone and siderite (chemofacies F, B), calcareous mudstone (chemofacies C, D and E) and limestone (chemofacies A) through the Bowland Shale Formation in Ellesmere Port-1 (Fig. 10). Importantly, differentiation of non-calcareous and calcareous mudstone facies helps to interpret the succession in the context of syngenetic processes (Fig. 9d-g), and ultimately, sequence stratigraphy. Based on the machine predictions, the Bowland Shale Formation comprises ca. 18% siltstone and sandstone, 37% non-calcareous mudstone, 42% calcareous mudstone and 3% limestone. The unit comprises 12 complete fourth order cycles, and is interfingered with the three distal Lower, Middle and Upper units (leaves) of the Cefn-y-fedw Sandstone Formation (Davies et al., 2004; Waters et al., 2020).

Using the ammonoid biozonation in the two core sections together with the known age ranges of each of the distal turbidite leaves of the Cefn-y-fedw Sandstone (Davies et al., 2004), it is possible to infer the key index regional marine bands (Davies et al., 2011) in the Blacon Basin. Like the observations in the core sections, generally sharp transitions from non-calcareous to calcareous mudstones are interpreted to indicate deposition during marine transgressions. 8 of the 12 cycles exhibit resolvable thin limestone beds, which likely coincide with the maximum rate of transgression and/or early part of the sea level highstand. Thus, the Blacon Basin apparently preserves a largely complete Namurian succession, analogous to the Craven Basin (Saunders and Ramsbottom, 1986). In all cycles, the calcareous mudstones are progressively or abruptly replaced with non-calcareous mudstones and/or siltstone to sandstone facies. We interpret these shifts from calcareous to siliciclastic facies to represent deposition during falling sea level, culminating in lowstands. The abrupt transitions from calcareous to non-calcareous mudstones are analogous to observations in core (Figs. 4-5); metre-scale cohesive debris flows shed from the basin margins. The lower, middle, and upper units of the Cefn-y-fedw Sandstone Formation plausibly occupy the lowstands of multiple cycles and are potentially associated with erosional basal surfaces that cut into the underlying strata. We interpret deposition of the middle Cefn-y-fedw Sandstone unit to span and/or to have incised through the entirety of the Alportian in the Blacon Basin. Thus, the mass transport deposit underlying the $H_{1a}1$ marine band in core 2 (Fig. 4) likely represents a precursor or the first pulse of the middle Cefn-y-fedw Sandstone unit. Similarly, the siltstone facies at the top of the Kinderscoutian section (core 1) is interpreted as the base of the upper Cefn-y-fedw Sandstone unit (Fig. 5).

We integrated the sequence stratigraphic interpretations, based upon the core scan observations and machine learning, with observations from other key wells in the Blacon Basin (Fig. 11). The results constrain the sedimentary architecture in the Blacon Basin. Ellesmere Port-1 is not located in the deepest part of the basin; it is located on the north-east flank of the basin. Taking a basin-wide perspective shows the importance and influence of the Cefyn-y-fedw delta system; except for the relatively thin marine band facies, the Bowland Shale in the Blacon Basin is relatively expanded and totally dominated by prodeltaic mud (Fig. 11). This is consistent with the dominance of Type III organic matter (including large plant fragments) in both core sections (Hennissen et al., this volume). This contrasts with the Bowland Shale in the Craven Basin; whilst also supplied by a large delta system, the succession in the Craven Basin represents deposition from a more balanced mixture of competing hemipelagic (biogenic) and allochthonous components (Clarke et al., 2018; Emmings et

ACCEPTED MANUSCRIPT

al., 2020a; Emmings et al., 2020b; Emmings et al., 2020c; Newport et al., 2018). The relatively expanded, clay-rich and poorly cemented mudstone succession (Fig. 6) is also in contrast to the economically important, broadly time-equivalent Barnett Shale Formation (Loucks and Ruppel, 2007). Ultimately, the structurally complex, collisional intercontinental setting explains why many of the US gas shales are poor analogues for the Bowland Shale. Structural complexity offers a direct challenge to unconventional hydrocarbon extraction from the Bowland Shale (Anderson and Underhill, 2020), but is also implicated in the compartmentalization of key cemented lithofacies and the encroachment of delta systems linked to an uplifting hinterland.

The stratigraphic analysis delineates an inflection point immediately above the middle Cefn-y-fedw Sandstone turbidite package at ca. 1615 m below surface, at or near the base of the Kinderscoutian (Fig. 10). The Pendleian and Arnsbergian cycles exhibit relatively low temporal frequency and a relatively low mean sediment accumulation rate (e.g., condensed) and are more strongly asymmetrical, suggestive of deposition under the combined influence of eustatic sea-level fluctuation and basin subsidence (e.g. Martinsen et al., 1995). During the Pendleian-Arnsbergian, Waters et al. (2020) showed detrital sediments entered the Blacon Basin via the Cefn-y-fedw delta systems in the south-west (Fig. 11). Sediment flows were potentially aligned parallel to the long axis of the combined Blacon and Widnes basins (Fig. 1), analogous to the Gainsborough Trough (Palci et al., 2020). Whilst the age of the middle Cefn-y-fedw Sandstone turbidite package is poorly constrained (Waters et al., 2020), it; (1) is potentially Chokerian, Alportian and/or earliest Kinderscoutian in age, and therefore must span or juxtapose one or more significant hiatuses; (2) overlies the $H_{1a}1$ biozone, and therefore likely occurs within the mid-Carboniferous (Mississippian-Pennsylvanian) eustatic event (Saunders and Ramsbottom, 1986), and; (3) is succeeded by a return to mud-dominated deposition in the early Kinderscoutian. Deposition of sand and presence of hiatuses is consistent with the development of protracted low eustatic sea level during the mid-Carboniferous event, which potentially shifted the main depocentres into deeper basins (e.g., the Craven Basin in the Irish Sea). Thus, the middle Cefn-y-fedw Sandstone *could* represent a turbidite lobe deposited during third-order sea level regression associated with the mid-Carboniferous eustatic event, although the role of local controls such as fault reactivation is unresolved.

The lithostratigraphic analysis shows the Blacon Basin became re-established as a major depocentre for mud during the Kinderscoutian. The well correlation together with heavy mineral analysis of Waters et al. (2020) suggests the Blacon Basin continued to receive detrital sediment from a single source via the Cefn-y-fedw delta system, located in the south or south-west. The Kinderscoutian to Yeodonian cycles apparently exhibit higher temporal frequency. Additionally, the Kinderscountian-Yeodonian succession was deposited under a relatively high mean sediment accumulation rate and the cycles are slightly more symmetrical, which likely reflects increasing proximity to the Cefn-y-fedw delta front (Fig. 11). By the Yeodonian, sediment supply into the Blacon Basin became more complex, with provenances from the south-west, south-east, north-west, and north-east (Waters et al., 2020).

Radiogenic heat productivity and heat flow

RHP calculations for the Bowland Shale in borehole Ellesmere Port-1 indicate bulk RHPs of 2.6 ±1.3 $\mu W/m^3$ (Fig. 12). Similarly high RHPs are also observed in Bowland Shale in the Craven Basin.

ACCEPTED MANUSCRIPT

The Bowland Shale RHPs are significantly higher than the global shale mean of ca. 1.5 $\mu W/m^3$ reported by Vilà et al. (2010), and approach the RHPs of granitic intrusions, targeted for geothermal energy in the UK (Gluyas et al., 2018). RHP derives from the decay of U, K, Th, in descending order of importance (Rybach, 1976). The U, K and Th data (Fig. 12c) indicate the high RHPs are primarily due to *relatively* high U concentrations, whereas Th and K concentrations are broadly in line with the global average. The U contents are relatively but not absolutely high; for example, the Alum Shale (Sweden) exhibits U concentrations between 100-300 ppm (Lecomte et al., 2017), an order of magnitude greater in comparison to the Bowland Shale.

The relatively high U in Carboniferous sedimentary rocks is additionally important because U can become mobile in groundwater or produced waters (Smedley et al., 2006), and the decay of U contributes to Rn risk areas where the rocks crop out (Miles et al., 2007). However, it should be noted the vast majority of UK groundwaters exhibit U concentrations far below the WHO provisional guideline value for U in drinking water (15 µg/L) (Smedley et al., 2006). Additionally, the relatively high U contents in UK groundwaters commonly derive from sandstone red-beds rather than Carboniferous shales, and U mobility is dependent on the mineral host and speciation (e.g., Smedley et al., 2006; Phan et al., 2015). In the Bowland Shale at a regional perspective, U is primarily hosted in recalcitrant mineral or organic phases (Parnell et al., this volume, see below) and is therefore likely to be relatively immobile.

The relatively high U contents observed in the Bowland Shale are potentially explained by three factors. Firstly, high U concentrations are a general feature of Devonian-Carboniferous shales globally (Mehra et al., 2021), suggesting a first order, fundamental change in the availability and/or fixation pathway of U in marine sediments during this time interval. Secondly, a productivity-driven model for anoxia and high mSARs related to proximity to multiple delta systems likely promoted under-consolidation of seabed sediments during deposition of the Bowland Shale. Since U is primarily fixed within porewaters rather than bottom waters (Tribovillard et al., 2006), under-consolidation could plausibly promote U drawdown due to generally enhanced shallow sediment porosity and diffusivity with bottom waters. Finally, the siltstone and sandstone facies in the Bowland Shale *also* exhibit high RHPs above the global sandstone average (Fig. 12). This strongly suggests an important role of provenance; granitic rocks were present in the hinterland (Waters et al., 2020) and the siltstones in Ellesmere Port-1 are compositionally immature, consistent with a granitic provenance. Specifically, silt and sand in the Bowland Shale is enriched in a suite of detrital minerals which are important hosts of U in granite (Nash, 1979), including heavy minerals, mica and especially detrital magnetite (Emmings et al., 2020c).

We modelled a range of scenarios using the heat flow box model equations of Beardsmore et al. (2010), assuming complete isotropy and negligible convective heat transport. Conductive heat flow is controlled by two parameters (Beardsmore et al., 2010); *in situ* RHP (Rybach, 1976) and the thermal conductivity of constituent phases. Carbonates, clay minerals and unsaturated or saturated pores are thermal insulators, whereas pyrite and quartz are important thermal conductors (Midttømme et al., 1998; Midttømme and Roaldset, 1999). The distribution of these phases in black shales is synergistically linked to redox conditions during deposition and diagenesis and is therefore predictable (Fig. 9) (Emmings et al., 2020b; Emmings et al., 2020c).

ACCEPTED MANUSCRIPT

The models show heat flow is highly sensitive to thermal conductivity and is minimally affected by RHP (Appendix B, see following discussion). Thus, black ('hot') shales are unlikely to represent a credible, direct target for geothermal energy. However, the Bowland Shale could act as an effective thermal blanket to underlying geothermal reservoirs (e.g., Nunn et al., 1999). This effect is potentially manifested as the Bowland Forest heat anomaly described by Lee et al. (1987), although the anomaly is not identified in more recent mapping (e.g., Busby, 2014). Maintaining the same arbitrary surface heat flow (50 W/m^2) and RHP (3 $\mu W/m^3$), box modelling shows the base of a 1 km-thick claystone unit is ca. 17°C warmer than at the base of a 1 km-thick siliceous, pyritic mudstone unit. This is because clay minerals are insulators whereas quartz and pyrite are conductors of heat. In these models, we assumed the same i*n situ* RHP of 3 $\mu W/m^3$ (Fig. 12b), which results in a relatively small excess temperature gradient of 0.75°C/km. However, adopting an *in situ* RHP of 10 $\mu W/m^3$ that is more comparable to high-RHP granite (Vilà et al., 2010), imparts an excess temperature gradient of 2°C/km. Thus, RHP becomes quantitively important where it is consistently high in a large rock volume (e.g., granite batholiths), a feature that is unlikely to be observed in sedimentary basins because it requires the presence of extremely thick metalliferous black shale packages. Whilst these modelling exercises are not entirely realistic, this approach helps to demonstrate the importance of understanding mudstone lithofacies as a control on subsurface heat flow.

In another exercise, we fitted two different, similarly accurate (but not necessarily realistic) temperature gradient models through the Bowland Shale in Ellesmere Port-1 (Fig. 13, Appendix B). Whilst the measured borehole temperatures in Ellesmere Port-1 are unlikely to be equilibrated with the surrounding rock, the data delineate the key inflection at ca. 1615 m interpreted related to the mid-Carboniferous eustatic event and delta progradation (see prior discussion). This inflection differentiates geothermal gradients of ca. 25°C/km and 18°C/km, respectively. Model 1 is based on a single, homogenous, low conductivity claystone package with low RHP (1.5 $\mu W/m^3$), 5 % total porosity (Clarke et al., 2018), 80 % clay minerals, 10 % quartz and 5 % carbonate minerals. Model 1 requires relatively low heat flows of 62 mW/m^2 and 42 mW/m^2, above and below 1615 m below surface, respectively, to match the observed borehole temperature profile. Model 2 is based on the calculated RHPs, and machine predicted thicknesses and composition of each discrete package within the Bowland Shale (Fig. 10, 13), and is therefore considered more realistic. In model 2, thermal conductivities are higher in all facies, which necessitate higher heat flows of 75 mW/m^2 and 55 mW/m^2, above and below 1615 m below surface, respectively. Thus, based on the observations coupled to modelling, the Bowland Shale in Ellesmere Port-1 is not necessarily an effective thermal 'blanket' since it comprises ca. 18% siltstone and sandstone, and instead may conduct heat at a faster rate (i.e., high thermal diffusivity) compared to pure claystones or condensed organic-rich shales. Again, these models are likely to be overly simplistic but demonstrate the importance of understanding the fractions of different mudstone facies within a given 'shale' package. The models do not consider the effect of organic matter (particularly coal) and are limited to the classes (lithologies) observed in the two cored sections. In particular, coals were not observed in either core section, but coal exhibits a very low thermal conductivity (Nunn and Lin, 2002) and coal seams are present in the Bowland Shale in North Wales (Davies et al., 2004).

The Blacon Basin, in addition to many other sedimentary basins, is filled by 100s m of Carboniferous mudstone. Important UK geothermal plays include granites (Gluyas et al., 2018) and karstified Carboniferous limestones (Busby, 2014). Carboniferous limestone-mudstone cyclothems cap granites on several blocks (e.g., proven in the Raydale and Rookhope boreholes; Dunham and

ACCEPTED MANUSCRIPT

Wilson, 1985) and cap lower Carboniferous limestones in the UK (e.g., Fig. 10; Dunham and Wilson, 1985; Busby, 2014). Additionally, basinal Carboniferous mudstones may cap granites beneath local intrabasin highs (Bott, 1988, Donato, 2020). Yet, our ability to explore for deep geothermal energy in sedimentary basins is limited by a lack of understanding of how different types of shales control heat flow. In addition, efficient heat diffusion is important for the safe geological storage of radioactive waste (Rutqvist, 2020), and the design of heat pumps is dependent on the thermal properties of the storage medium (Busby et al., 2009; Parkes et al., 2020). Simple box modelling together with previous work (e.g., Midttømme et al., 1998) shows the efficiency of the sedimentary thermal blanket is highly dependent on mudstone mineralogy – and by extension – lithofacies. Therefore, future work should seek to (1) measure the key thermal properties for a range of mudstone microfacies; (2) better understand the role of depositional processes, basin type and age as controls on mudstone facies coupled to thermal conductivity; (3) constrain the effect of diagenesis on mudstone thermal properties; (4) link the thermal properties of mudstones to one or more holistic, predictive frameworks (e.g., sequence stratigraphy); (5) investigate the potential for convective fluid flow through fracture networks, which are more likely to be developed within relatively brittle mudstone microfacies (e.g., siliceous and carbonate-cemented marine band facies).

Conclusions

We conducted a high-resolution multi-disciplinary analysis of two core sections in the borehole Ellesmere Port-1, Cheshire, UK. Biostratigraphic analysis indicates the core sections are Kinderscoutian and late Arnsbergian-Chokerian in age, respectively. Both cores are assigned to the Bowland Shale Formation. Coupled core scan and discrete geochemical analysis enables interpretation of syngenetic processes at a relatively high temporal resolution (ca. 1-2 kyrs). Both cores comprise cycles of limestone, calcareous to non-calcareous mudstone and siltstone that is characteristic of the Bowland Shale in the UK. The cycles are interpreted to represent sediment deposition during fourth-order, glacioeustatic sea level fluctuation. Palaeoredox and palaeosalinity geochemical proxies support a model for productivity-driven anoxia in a weakly restricted basin. Coupled Mo/Al and As/Al core scan ratios support a model for intermittently euxinic bottom waters overlain by relatively thick ferruginous intermediate waters. Falling sea level led to the waning of marine productivity; euxinic bottom waters were progressively replaced with ferruginous waters, followed by the development of fully suboxic or oxic conditions during the late falling stage and lowstands.

Unlike the Pendleain Bowland Shale in the Craven Basin, the cored Bowland Shale successions in Ellesmere Port-1 are not siliceous and are instead dominated by argillaceous mudstones. Marine band facies are interpreted to represent deposition during marine transgressions and highstands. Falling sea level is linked to the progressive or abrupt replacement of calcareous mudstones with siliciclastic (non-carbonate-bearing) claystones. The siliciclastic mudstones are commonly laminated and often exhibit chaotic sedimentary structures, suggestive of deposition from a range of density flow types, including potential for en masse transport within debris flows. Laminated siltstone and sandstone packages occasionally cap the siliciclastic claystones and are interpreted to represent deposition during lowstands, where bottom water conditions were unambiguously oxygenated, brackish and at least intermittently freshwater.

ACCEPTED MANUSCRIPT

Cluster analysis of the XRF core scan data coupled to machine learning of the well log data enabled prediction of limestone, calcareous mudstone, siliciclastic (non-carbonate) claystone, and siltstone and sandstone facies through the entire Bowland Shale interval in Ellesmere Port-1. The machine predictions show the Bowland Shale is interfingered with the three turbiditic leaves of the Cefn-y-fedw Sandstone and contains 12 complete fourth-order cycles resolvable in the well log data. The Bowland Shale comprises ca. 18% siltstone and sandstone, 37% non-calcareous mudstone, 42% calcareous mudstone and 3% limestone. A step-change in the symmetry and thickness of cycles at ca. 1615 m below surface likely corresponds to an important regional shift in the rate of sediment supply from the Cefn-y-fedw delta system, above the mid-Carboniferous boundary.

The Bowland Shale exhibits high RHP in comparison to other sedimentary rocks, due primarily to relative enrichment in U. Despite this, box model heat modelling calibrated to borehole temperature measurements show heat flow is minimally influenced by the high RHP in the Bowland Shale. Modelling suggests it is not necessarily appropriate to assume that the Bowland Shale is an insulating 'blanket' to subsurface heat flow. Simple box modelling shows the efficiency of the sedimentary thermal blanket is highly dependent on mudstone mineralogy and facies. The Bowland Shale in the Blacon Basin is relatively expanded and does not represent a highly condensed black shale unit. Based on the compositional (XRF) analysis, the Bowland Shale microfacies in the UK are likely to be more conductive than a simple claystone lithology. Considering the potential importance of Carboniferous mudstones as caprocks to buried granite and limestone geothermal plays in the UK, further work should (1) measure the thermal properties of a range of mudstone microfacies; (2) link the findings to established depositional and lithostratigraphic models, to better understand the extent to which mudstone units act as thermal blankets.

ACCEPTED MANUSCRIPT

Acknowledgements

This research was primarily funded by a British Geological Survey (UKRI) National Capability grant NEE6640S (to JFE). JAIH is supported by the Natural Environment Research Council through the Unconventional Hydrocarbons in the UK Energy System Programme (UKUH) Challenge 2 (NE/R017964/1). Stable C isotope analyses were funded by the NEIF Steering Committee [grant no. IP-1918-0619] (to MJL). We acknowledge the National Geoscience Data Centre (NGDC), British Geological Survey for enabling access to the Ellesmere Port-1 core materials. We acknowledge Mike Stephenson (formerly BGS) for helping to facilitate the research project. We thank Simon Harris (BGS) and Sarah Davies (University of Leicester) for facilitating access to laboratory facilities at the NGDC and the University of Leicester XRF laboratory, respectively. Contains data supplied by permission of the Natural Environment Research Council [2022]. Contains information provided by the Oil and Gas Authority and/or other third parties.

Author contributions

CREDIT author statement:

JFE – conceptualization, methodology, formal analysis, data curation, writing – original draft, writing – review and editing, visualization

JAIH - methodology, formal analysis, data curation, writing – review and editing, visualization

CHV - formal analysis, resources, supervision

MD – formal analysis, data curation, writing – original draft, resources

LM – formal analysis

VMH – formal analysis

AL – formal analysis, writing – original draft

JL – formal analysis, writing – original draft

MJL – resources, supervision, funding acquisition

NR – formal analysis, writing – review and editing

Data availability

All discrete sample geochemical datasets (RockEval pyrolysis, XRF elemental analysis, stable C and S isotopes) are reported in the appendices. The XRF core scan datataset is archived and openly available via the NDGC (BGS Core Scanning Facility, 2022). The Ellesmere Port-1 cores are openly available via the National Geoscience Data Centre (NGDC), British Geological Survey. Well log data are available via the National Data Repository (https://www.nstauthority.co.uk/data-centre/access-to-information-and-samples/). The palynology and vitrinite reflectance datasets are reported by Hennissen et al. (this volume).

ACCEPTED MANUSCRIPT

References

Aitchison, J., 1986. The Statistical Analysis of Compositional Data. Monographs on Statistics and Applied Probability. Chapman & Hall Ltd, London, 416 pp.

Algeo, T., Heckel, P.H., Maynard, J.B., Blakey, R., Rowe, H., 2008. Modern and Ancient Epeiric Seas and the Super-Estuarine Circulation Model of Marine Anoxia. In: Pratt, Holmden (Eds.), Special Paper 48: Dynamics of Epeiric Seas, pp. 7-38.

Algeo, T.J., 2004. Can marine anoxic events draw down the trace element inventory of seawater? Geology, 32(12): 1057-1060.

Algeo, T.J., Lyons, T.W., 2006. Mo–total organic carbon covariation in modern anoxic marine environments: Implications for analysis of paleoredox and paleohydrographic conditions. Paleoceanography, 21(1): n/a-n/a.

Algeo, T.J., Tribovillard, N., 2009. Environmental analysis of paleoceanographic systems based on molybdenum–uranium covariation. Chemical Geology, 268(3–4): 211-225.

Anderson, I., Underhill, J.R., 2020. Structural constraints on Lower Carboniferous shale gas exploration in the Craven Basin, NW England. Petroleum Geoscience, 26(2): 303-324.

Andrews, I.J., 2013. The Carboniferous Bowland Shale gas study: geology and resource estimation. British Geological Survey for Department of Energy and Climate Change.

Arthurton, R.S., 1984. The Ribblesdale fold belt, NW England—a Dinantian-early Namurian dextral shear zone. Geological Society, London, Special Publications, 14(1): 131-138.

Auguie, B., 2016. gridExtra: Miscellaneous Functions for "Grid" Graphics. R package version 2.2.1. https://CRAN.R-project.org/package=gridExtra.

Baines, J.G., 1977. The Stratigraphy and Sedimentology of the Skipton Moor Grits (Namurian E1c) and Their Lateral Equivalents. Unpublished PhD Thesis, University of Keele.

Beardsmore, G., Rybach, L., Blackwell, D., Baron, C., 2010. A protocol for estimating and mapping global EGS potential. GRC Trans, 34: 301-312.

Berner, R.A., Raiswell, R., 1984. C/S method for distinguishing freshwater from marine sedimentary rocks. Geology, 12(6): 365-368.

BGS Core Scanning Facility, 2022. Ellesmere Port-1 Core Scanning Dataset. NERC EDS National Geoscience Data Centre. (Dataset). .

Bloxam, T.W., Thomas, R.L., 1968. Palaeontological and geochemical facies in the Gastrioceras subcrenatum marine-band and associated rocks from the North Crop of the South Wales Coalfield. Quarterly Journal of the Geological Society, 124(1-4): 239-277.

Bott, M.H.P., 1988. The Market Weighton gravity anomaly; granite or graben? Proceedings of the Yorkshire Geological Society, 47(1): 47-53.

Bouch, J.E. et al., 2006. Direct evidence of fluid mixing in the formation of stratabound Pb–Zn–Ba–F mineralisation in the Alston Block, North Pennine Orefield (England). Mineralium Deposita, 41(8): 821-835.

Brandon, A., Riley, N.J., Wilson, A.A., Ellison, R.A., 1995. Three new early Namurian (E1c-E2a) marine bands in central and northern England, UK, and their bearing on correlations with the Askrigg Block. Proceedings of the Yorkshire Geological and Polytechnic Society, 50(4): 333-355.

Brogan, J.C., Fleming, G.A., Byrne, J.E., 1973. Molybdenum and Copper in Irish Pasture Soils. Irish Journal of Agricultural Research, 12(1): 71-81.

Busby, J., Lewis, M., Reeves, H., Lawley, R., 2009. Initial geological considerations before installing ground source heat pump systems. Quarterly Journal of Engineering Geology and Hydrogeology, 42(3): 295-306.

Busby, J., 2014. Geothermal energy in sedimentary basins in the UK. Hydrogeology Journal, 22(1): 129-141.

Busby, J., Terrington, R., 2017. Assessment of the resource base for engineered geothermal systems in Great Britain. Geothermal Energy, 5(1): 7.

ACCEPTED MANUSCRIPT

Church, K.D., Gawthorpe, R.L., 1994. High resolution sequence stratigraphy of the late Namurian in the Widmerpool Gulf (East Midlands, UK). Marine and Petroleum Geology, 11(5): 528-544.
Clarke, H., Turner, P., Bustin, R.M., Riley, N., Besly, B., 2018. Shale gas resources of the Bowland Basin, NW England: a holistic study. Petroleum Geoscience, 24(3): 287-322.
Clarke, H., Verdon, J.P., Kettlety, T., Baird, A.F., Kendall, J.M., 2019. Real-Time Imaging, Forecasting, and Management of Human-Induced Seismicity at Preston New Road, Lancashire, England. Seismological Research Letters, 90(5): 1902-1915.
Cózar, P., Somerville, I.D., 2021. The Serpukhovian in Britain: use of foraminiferal assemblages for dating and correlating. Journal of the Geological Society: jgs2020-170.
Davies, J.R., Wilson, D., Williamson, I.T., 2004. Geology of the country around Flint. Memoirs of the British Geological Survey, Sheet 108 (England and Wales).
Davies, J.R., Somerville, I.D., Waters, C.N., Jones, N.S., 2011. North Wales. In: Waters, C.N. et al. (Eds.), A Revised Correlation of Carboniferous Rocks in the British Isles. Geological Society of London, pp. 0.
Davies, R.J., Austin, R., Moore, D., 1993. Environmental controls of Brigantian conodont-distribution: evidence from the Gayle limestone of the Yoredale Group in Northern England. Annales de la Société géologique de Belgique, 116(Fascicule 2 - Carboniferous biostratigraphy): 221-241.
Davies, S., Hampson, G., Flint, S., Elliott, T., 1999. Continental-scale sequence stratigraphy of the Namurian, Upper Carboniferous and its applications to reservoir prediction. Geological Society, London, Petroleum Geology Conference Series, 5: 757-770.
Davies, S.J., 2008. The record of Carboniferous sea-level change in low-latitude sedimentary successions from Britain and Ireland during the onset of the late Paleozoic ice age. Geological Society of America Special Papers, 441: 187-204.
Davydov, V.I., Korn, D., Schmitz, M., 2012. The Carboniferous Period. Geologic Time Scale 2012 2-Volume Set. Elsevier.
DECC, 2013. Department for Energy and Cimate Change, The Hydrocarbon Prospectivity of Britain's Onshore Basins.
Dmitrijeva, M. et al., 2020. Multivariate Statistical Analysis of Trace Elements in Pyrite: Prediction, Bias and Artefacts in Defining Mineral Signatures. Minerals, 10(1): 61.
Donato, J., 2020. Gravity modelling across two postulated granite batholiths within the UK onshore East Midlands Shelf, University of Oxford/UKOGL Beneath Britain Website.
Dowey, P.J., Taylor, K.G., 2019. Diagenetic mineral development within the Upper Jurassic Haynesville-Bossier Shale, USA. Sedimentology.
Dowle, M., Srinivasan, A., 2020. data.table: Extension of `data.frame`. R package version 1.13.2. https://CRAN.R-project.org/package=data.table.
Droxler, A.W., Schlager, W., 1985. Glacial versus interglacial sedimentation rates and turbidite frequency in the Bahamas. Geology, 13(11): 799-802.
Dunham, A.C., Wilson, A.A., 1985. Geology of the Northern Pennine Orefield: Volume 2, Stainmore to Craven. . Economic Memoir of the British Geological Survey.
Ellis, D., Singer, J., 2007. Well Logging for Earth Scientists. Springer, Dordrecht.
Emmings, J.F., 2018. Controls on UK Lower Namurian Shale Gas Prospectivity: Understanding the Spatial and Temporal Distribution of Organic Matter in Siliciclastic Mudstones. PhD Thesis, University of Leicester.
Emmings, J.F. et al., 2019. Controls on amorphous organic matter type and sulphurization in a Mississippian black shale. Review of Palaeobotany and Palynology, 268: 1-18.
Emmings, J.F., Davies, S., Vane, C.H., Moss-Hayes, V., Stephenson, M., 2020a. From marine bands to hybrid flows: Sedimentology of a Mississippian black shale. Sedimentology, 67(1): 261-304.
Emmings, J.F. et al., 2020b. Origin and implications of early diagenetic quartz in the Mississippian Bowland Shale Formation, Craven Basin, UK. Marine and Petroleum Geology, 120.
Emmings, J.F. et al., 2020c. A Mississippian black shale record of redox oscillation in the Craven Basin, UK. Palaeogeography, Palaeoclimatology, Palaeoecology, 538.
ACCEPTED MANUSCRIPT

Emmings, J.F. et al., 2022. Pyrite mega-analysis reveals modes of anoxia through geological time. Science Advances, 8(11): eabj5687.
Fauchille, A.L. et al., 2017. An enhanced understanding of the Basinal Bowland shale in Lancashire (UK), through microtextural and mineralogical observations. Marine and Petroleum Geology, 86: 1374-1390.
Fauchille, A.L. et al., 2018. Variability in spatial distribution of mineral phases in the Lower Bowland Shale, UK, from the mm- to µm-scale: Quantitative characterization and modelling. Marine and Petroleum Geology, 92: 109-127.
Fisher, Q.J., Wignall, P.B., 2001. Palaeoenvironmental controls on the uranium distribution in an Upper Carboniferous black shale (Gastrioceras listeri Marine Band) and associated strata; England. Chemical Geology, 175(3): 605-621.
Fraser, A.J., Gawthorpe, R.L., 1990. Tectono-stratigraphic development and hydrocarbon habitat of the Carboniferous in northern England. Geological Society of London Special Publication, 55(1): 49-86.
Fraser, A.J., Nash, D.F., Steele, R.P., Ebdon, C.C., Fraser, A.J., 1990. A regional assessment of the intra-Carboniferous play of Northern England. Geological Society, London, Special Publications, 50(1): 417-440.
Fraser, A.J., Gawthorpe, R., 2003. An Atlas of Carboniferous Basin Evolution in Northern England. Memoir 28. Geological Society, London.
Gadd, M.G. et al., 2020. A Middle Devonian basin-scale precious metal enrichment event across northern Yukon (Canada). Geology, 48(3): 242-246.
Gluyas, J. et al., 2018. Keeping warm: a review of deep geothermal potential of the UK. Proceedings of the Institution of Mechanical Engineers, Part A: Journal of Power and Energy, 232(1): 115-126.
Green, P.F., Duddy, I.R., Bray, R.J., 1997. Variation in thermal history styles around the Irish Sea and adjacent areas: implications for hydrocarbon occurrence and tectonic evolution. Geological Society, London, Special Publications, 124(1): 73-93.
Gross, D. et al., 2015. Organic geochemistry of Mississippian shales (Bowland Shale Formation) in central Britain: Implications for depositional environment, source rock and gas shale potential. Marine and Petroleum Geology, 59(0): 1-21.
Hamilton, N., 2017. ggtern: An Extension to 'ggplot2', for the Creation of Ternary Diagrams. R package version 2.2.1. https://CRAN.R-project.org/package=ggtern.
Hampson, G.J., 1997. A sequence stratigraphic model for deposition of the Lower Kinderscout Delta, an Upper Carboniferous turbidite-fronted delta. Proceedings of the Yorkshire Geological and Polytechnic Society, 51(4): 273-296.
Hennissen, J.A.I. et al., 2017. The prospectivity of a potential shale gas play: An example from the southern Pennine Basin (central England, UK). Marine and Petroleum Geology, 86: 1047-1066.
Hild, E., Brumsack, H.J., 1998. Major and minor element geochemistry of Lower Aptian sediments from the NW German Basin (core Hohenegglesen KB 40). Cretaceous Research, 19(5): 615-633.
Holdsworth, B., Collinson, J.D., 1988. Millstone Grit cyclicity revisited. In: Besly, B.M., Kelling, G. (Eds.), Sedimentation in a Synorogenic Basin Complex: The Upper Carboniferous of Northwest Europe. Blackie, Glasgow, pp. 132 - 152.
Hollis, C., Walkden, G., 2012. Burial diagenetic evolution of the Lower Carboniferous (Dinantian) of the southern margin of the Askrigg Platform and a comparison with the Derbyshire Platform. Petroleum Geoscience, 18(1): 83-95.
IPCC, 2014. Climate Change 2014: Synthesis Report. Contribution of Working Groups I, II and III to the Fifth Assessment Report of the Intergovernmental Panel on Climate Change. IPCC, Geneva, Switzerland, 151 pp.

ACCEPTED MANUSCRIPT

Jackson, D.I., Johnson, H., Smith, N.J.P., 1997. Stratigraphical relationships and a revised lithostratigraphical nomenclature for the Carboniferous, Permian and Triassic rocks of the offshore East Irish Sea Basin. Geological Society, London, Special Publications, 124(1): 11-32.

Jarvie, D.M., 2012a. Shale resource systems for oil and gas: Part 1 - Shale-gas resource systems. Shale reservoirs - Giant resources for the 21st century: AAPG Memoir 97.

Jarvie, D.M., 2012b. Shale resource systems for oil and gas: Part 2 - Shale-oil resource systems. Shale reservoirs - Giant resources for the 21st century: AAPG Memoir 97.

Juerges, A., Hollis, C.E., Marshall, J., Crowley, S., 2015. The control of basin evolution on patterns of sedimentation and diagenesis: an example from the Mississippian Great Orme, North Wales. Journal of the Geological Society.

Kabanov, P., Jiang, C., 2020. Photic-zone euxinia and anoxic events in a Middle-Late Devonian shelfal sea of Panthalassan continental margin, NW Canada: Changing paradigm of Devonian ocean and sea level fluctuations. Global and Planetary Change, 188: 103153.

Kampschulte, A., Bruckschen, P., Strauss, H., 2001. The sulphur isotopic composition of trace sulphates in Carboniferous brachiopods: implications for coeval seawater, correlation with other geochemical cycles and isotope stratigraphy. Chemical Geology, 175(1): 149-173.

Kampschulte, A., Strauss, H., 2004. The sulfur isotopic evolution of Phanerozoic seawater based on the analysis of structurally substituted sulfate in carbonates. Chemical Geology, 204(3): 255-286.

Kendrick, M.A., Burgess, R., Pattrick, R.A.D., Turner, G., 2002. Hydrothermal Fluid Origins in a Fluorite-Rich Mississippi Valley-Type District: Combined Noble Gas (He, Ar, Kr) and Halogen (Cl, Br, I) Analysis of Fluid Inclusions from the South Pennine Ore Field, United Kingdom. Economic Geology, 97(3): 435-451.

Kerschke, D., Schulz, H.-M., 2013. The shale gas potential of Tournaisian, Visean, and Namurian black shales in North Germany: baseline parameters in a geological context. Environmental Earth Sciences, 70(8): 3817-3837.

Kidder, D.L., Worsley, T.R., 2010. Phanerozoic Large Igneous Provinces (LIPs), HEATT (Haline Euxinic Acidic Thermal Transgression) episodes, and mass extinctions. Palaeogeography, Palaeoclimatology, Palaeoecology, 295(1): 162-191.

Kirkham, A., 2021. Mass collapse and resedimentation on a Brigantian–Early Namurian platform margin, Halkyn–Mold area, North Wales, UK. Geological Journal, n/a(n/a).

Könitzer, S.F., Davies, S., Stephenson, M., Leng, M., 2014. Depositional controls on mudstone lithofacies in a basinal setting: implications for the delivery of sedimentary organic matter. Journal of Sedimentary Research, 84(3): 198 - 214.

Könitzer, S.F., Stephenson, M.H., Davies, S.J., Vane, C.H., Leng, M.J., 2016. Significance of sedimentary organic matter input for shale gas generation potential of Mississippian Mudstones, Widmerpool Gulf, UK. Review of Palaeobotany and Palynology, 224, Part 2: 146-168.

Kuhn, M., 2020. caret: Classification and Regression Training. R package version 6.0-86. https://CRAN.R-project.org/package=caret.

Lafargue, E., Marquis, F., Pillot, D., 1998. Rock-Eval 6 Applications in Hydrocarbon Exploration, Production, and Soil Contamination Studies. Rev. Inst. Fr. Pét., 53(4): 421-437.

Lecomte, A., Cathelineau, M., Michels, R., Peiffert, C., Brouand, M., 2017. Uranium mineralization in the Alum Shale Formation (Sweden): Evolution of a U-rich marine black shale from sedimentation to metamorphism. Ore Geology Reviews, 88: 71-98.

Lee, M.K., Brown, G.C., Webb, P.C., Whieldon, J., Rollin, K.E., 1987. Heat flow, heat production and thermo-tectonic setting in mainland UK. Journal of the Geological Society, 144(1): 35-42.

Leeder, M., Raiswell, R., Al-Biatty, H., Mcmahon, A., Hardman, M., 1990. Carboniferous stratigraphy, sedimentation and correlation of well 48/3-3 in the southern North Sea Basin: integrated use of palynology, natural gamma/sonic logs and carbon/sulphur geochemistry. Journal of the Geological Society, 147(2): 287-300.

ACCEPTED MANUSCRIPT

Leeder, M.R., 1982. Upper Palaeozoic basins of the British Isles—Caledonide inheritance versus Hercynian plate margin processes. Journal of the Geological Society, 139(4): 479-491.
Lewan, M.D., 1986. Stable carbon isotopes of amorphous kerogens from Phanerozoic sedimentary rocks. Geochimica et Cosmochimica Acta, 50(8): 1583-1591.
Lindgreen, H., 1994. Ammonium fixation during illite-smectite diagenesis in Upper Jurassic shale, North Sea. Clay Minerals, 29(4): 527-537.
Loucks, R., Ruppel, S., 2007. Mississippian Barnett Shale: Lithofacies and depositional setting of a deep-water shale-gas succession in the Fort Worth Basin, Texas. AAPG Bulletin, 91(4): 579-601.
Loveless, S.E. et al., 2018. Characterising the vertical separation of shale-gas source rocks and aquifers across England and Wales (UK). Hydrogeology Journal, 26(6): 1975-1987.
Magraw, D., Ramsbottom, W.H.C., 1957. A deep borehole for oil at croxteth park, near liverpool. Geological Journal, 1(6): 512-535.
Martinsen, O.J., Collinson, J.D., Holdsworth, B.K., 1995. Millstone Grit Cyclicity Revisited, II: Sequence Stratigraphy and Sedimentary Responses to Changes of Relative Sea-Level, Sedimentary Facies Analysis. Blackwell Publishing Ltd., pp. 305-327.
Maynard, J.R., Wignall, P.B., Varker, W.J., 1991. A 'hot' new shale facies from the Upper Carboniferous of Northern England. Journal of the Geological Society, 148(5): 805-808.
Maynard, J.R., Leeder, M.R., 1992. On the periodicity and magnitude of Late Carboniferous glacio-eustatic sea-level changes. Journal of the Geological Society, 149(3): 303-311.
Mazzini, A. et al., 2004. Methane-related authigenic carbonates from the Black Sea: geochemical characterisation and relation to seeping fluids. Marine Geology, 212(1): 153-181.
Mehra, A. et al., 2021. Curation and analysis of global sedimentary geochemical data to inform Earth history. GSA Today, 31.
Mercuzot, M. et al., 2021. Carbon and Nitrogen Cycle Dynamic in Continental Late-Carboniferous to Early Permian Basins of Eastern Pangea (Northeastern Massif Central, France). Frontiers in Earth Science, 9.
Meyer, K.M., Kump, L.R., 2008. Oceanic Euxinia in Earth History: Causes and Consequences. Annual Review of Earth and Planetary Sciences, 36(1): 251-288.
Meyers, P.A., 1994. Preservation of elemental and isotopic source identification of sedimentary organic matter. Chemical Geology, 114(3): 289-302.
Midttømme, K., Roaldset, E., Aagaard, P., 1998. Thermal conductivity of selected claystones and mudstones from England. Clay Minerals, 33(1): 131-145.
Midttømme, K., Roaldset, E., 1999. Thermal conductivity of sedimentary rocks: uncertainties in measurement and modelling. Geological Society, London, Special Publications, 158(1): 45-60.
Miles, J. et al., 2007. Indicative Atlas of Radon in England and Wales, Health Protection Agency and the British Geological Survey, HPA-RPD-033.
Mitchum, R.M., Van Wagoner, J.C., 1991. High-frequency sequences and their stacking patterns: sequence-stratigraphic evidence of high-frequency eustatic cycles. Sedimentary Geology, 70(2): 131-160.
Monaghan, A.A., Underhill, J.R., Marshall, J.E.A., Hewett, A.J., 2019. Paleozoic plays of NW Europe: an introduction. Geological Society, London, Special Publications, 471(1): 1-15.
Morton, A., Waters, C., Fanning, M., Chisholm, I., Brettle, M., 2015. Origin of Carboniferous sandstones fringing the northern margin of the Wales-Brabant Massif: insights from detrital zircon ages. Geological Journal, 50(5): 553-574.
Mossmann, J.-R., Aplin, A.C., Curtis, C.D., Coleman, M.L., 1991. Geochemistry of inorganic and organic sulphur in organic-rich sediments from the Peru Margin. Geochimica et Cosmochimica Acta, 55(12): 3581-3595.
Nash, T., 1979. Uranium and thorium in granitic rocks of northeastern Washington and northern Idaho, with comments on uranium resource potential, USGS Open-File Report 79-233

ACCEPTED MANUSCRIPT

Newport, L.P., Aplin, A.C., Gluyas, J.G., Greenwell, H.C., Gröcke, D.R., 2016. Geochemical and lithological controls on a potential shale reservoir: Carboniferous Holywell Shale, Wales. Marine and Petroleum Geology, 71(C): 198-210.

Newport, S.M., Jerrett, R.M., Taylor, K.G., Hough, E., Worden, R.H., 2018. Sedimentology and microfacies of a mud-rich slope succession: in the Carboniferous Bowland Basin, NW England (UK). Journal of the Geological Society, 175(2): 247-262.

Newport, S.M., 2019. The Bowland Shale (UK): development of new sedimentological and diagenetic models for a Palaeozoic fine-grained succession, University of Manchester.

Nunn, J.A., Lin, G., Zhang, L., 1999. Thermal Insulation by Low Thermal Conductivity Shales: Implications for Basin-Scale Fluid Flow and Heat Transport. In: Förster, A., Merriam, D.F. (Eds.), Geothermics in Basin Analysis. Springer US, Boston, MA, pp. 117-130.

Nunn, J.A., Lin, G., 2002. Insulating effect of coals and organic rich shales: implications for topography-driven fluid flow, heat transport, and genesis of ore deposits in the Arkoma Basin and Ozark Plateau. Basin Research, 14(2): 129-145.

Palci, F. et al., 2020. Shale oil and gas resource evaluation through 3D basin and petroleum systems modelling: a case study from the East Midlands, onshore UK. Petroleum Geoscience, 26(4): 525-543.

Parkes, D., Busby, J., Kemp, S.J., Petitclerc, E., Mounteney, I., 2020. The thermal properties of the Mercia Mudstone Group. Quarterly Journal of Engineering Geology and Hydrogeology: qjegh2020-098.

Parnell, J., Swainbank, I., 1990. Pb-Pb dating of hydrocarbon migration into a bitumen-bearing ore deposit, North Wales. Geology, 18(10): 1028-1030.

Parnell, J., Brolly, C., Spinks, S., Bowden, S., 2016. Selenium enrichment in Carboniferous Shales, Britain and Ireland: Problem or opportunity for shale gas extraction? Applied Geochemistry, 66: 82-87.

Patruno, S., Helland-Hansen, W., 2018. Clinoforms and clinoform systems: Review and dynamic classification scheme for shorelines, subaqueous deltas, shelf edges and continental margins. Earth-Science Reviews, 185: 202-233.

Pearce, T.J., McLean, D., Martin, J.H., Ratcliffe, K., Wray, D., 2010. A whole-rock geochemical approach to the recognition and correlation of "marine bands. In: Ratcliffe, K., Zaitlin, B. (Eds.), Application of Modern Stratigraphic Techniques: Theory and Case Histories. SEPM (Society for Sedimentary Geology), pp. 221-238.

Pellegrini, C. et al., 2017. How to make a 350-m-thick lowstand systems tract in 17,000 years: The Late Pleistocene Po River (Italy) lowstand wedge. Geology, 45(4): 327-330.

Peters-Kottig, W., Strauss, H., Kerp, H., 2006. The land plant δ13C record and plant evolution in the Late Palaeozoic. Palaeogeography, Palaeoclimatology, Palaeoecology, 240(1–2): 237-252.

Peters, S., Loss, D., 2012. Storm and fair-weather wave base: A relevant distinction? Geology, 40(6): 511-514.

Phan, T.T. et al., 2015. Trace metal distribution and mobility in drill cuttings and produced waters from Marcellus Shale gas extraction: Uranium, arsenic, barium. Applied Geochemistry, 60: 89-103.

Pharaoh, T. et al., 2019a. The Môn-Deemster-Ribblesdale Fold-Thrust Belt, Central UK: a concealed variscan inversion belt located on weak caledonian crust. Geological Society, London, Special Publications, 490: SP490-2018-109.

Pharaoh, T.C. et al., 2019b. An overlooked play? Structure, stratigraphy and hydrocarbon prospectivity of the Carboniferous in the East Irish Sea–North Channel basin complex. Geological Society, London, Special Publications, 471(1): 281-316.

R, Core Team, 2018. R: A language and environment for statistical computing. R Foundation for Statistical Computing, Vienna, Austria. . https://www.R-project.org.

Raiswell, R., Berner, R.A., 1987. Organic carbon losses during burial and thermal maturation of normal marine shales. Geology, 15(9): 853-856.

ACCEPTED MANUSCRIPT

Ramsbottom, W.H.C., Rhys, G.J., Smith, E.G., 1962. Boreholes in the Carboniferous rocks of the Ashover district, Derbyshire,. Bulletin of the Geological Survey of Great Britain, 19: 75-168.
Ramsbottom, W.H.C., 1977. Major cycles of transgression and regression (mesothems) in the Namurian. Proceedings of the Yorkshire Geological and Polytechnic Society, 41(3): 261-291.
Ramsbottom, W.H.C., 1979. Rates of transgression and regression in the Carboniferous of NW Europe. Journal of the Geological Society, 136: 147 - 153.
Ramsbottom, W.H.C., Saunders, W.B., 1985. Evolution and Evolutionary Biostratigraphy of Carboniferous Ammonoids. Journal of Paleontology, 59(1): 123-139.
Riley, D.A., Pearce, T.J., Mathia, E., Ratcliffe, K., Martin, J., 2016. The application of elemental geochemistry to UK onshore unconventional plays. Geological Society, London, Petroleum Geology Conference series, 8.
Rollin, K., 2002. Assessment of BGS data for ground source heat pump installations in the UK. British geological survey internal report, IR/02/196.
Rutqvist, J., 2020. Thermal management associated with geologic disposal of large spent nuclear fuel canisters in tunnels with thermally engineered backfill. Tunnelling and Underground Space Technology, 102: 103454.
Rybach, L., 1976. Radioactive heat production: a physical property determined by the chemistry of rocks, The physics and chemistry of minerals and rocks. Wiley, London, pp. 309-318.
Rygel, M.C., Fielding, C.R., Frank, T.D., Birgenheier, L.P., 2008. The Magnitude of Late Paleozoic Glacioeustatic Fluctuations: A Synthesis. Journal of Sedimentary Research, 78(8): 500-511.
Saunders, W.B., Ramsbottom, W.H.C., 1986. The mid-Carboniferous eustatic event. Geology, 14(3): 208-212.
Schuster, A., Strehlow, B.W., Eckford-Soper, L., McAllen, R., Canfield, D.E., 2021. Effects of Seasonal Anoxia on the Microbial Community Structure in Demosponges in a Marine Lake in Lough Hyne, Ireland. mSphere, 6(1): e00991-20.
Shanmugam, G., Moiola, R.J., 1982. Eustatic control of turbidites and winnowed turbidites. Geology, 10(5): 231-235.
Smedley, P.L., Smith, B., Abesser, C., Laptworth, D., 2006. Uranium occurrence and behaviour in British groundwater, British Geological Survey Commissioned Report, CR/06/050N. 60 pp. .
Smith, N., Kirby, G.A., Pharaoh, T.C., Hulbert, A.G., Shaw, K., 2005. Structure and evolution of the south-west Pennine Basin and adjacent areas : subsurface memoir, British Geological Survey.
Somerville, I.D., 1979. A cyclicity in the early Brigantian (D2) limestones east of the Clwydian Range, North Wales and its use in correlation. Geological Journal, 14(1): 69-86.
Spears, D.A., Kanaris-Sotiriou, R., Riley, N., Krause, P., 1999. Namurian bentonites in the Pennine Basin, UK – origin and magmatic affinities. Sedimentology, 46(2): 385-401.
Talling, P., Masson, D., Sumner, E., Malgesini, G., 2012. Subaqueous Sediment Density Flows: Depositional Processes and Deposit Types. Sedimentology, 59: 1937 - 2003.
Tissot, B., Welte, D., 1984. Petroleum Formation and Occurrence. Springer-Verlag.
Tribovillard, N., Algeo, T., Lyons, T., Riboulleau, A., 2006. Trace metals as paleoredox and paleoproductivity proxies: An update. Chemical Geology, 232: 12 - 32.
Tribovillard, N., Algeo, T.J., Baudin, F., Riboulleau, A., 2012. Analysis of marine environmental conditions based on molybdenum–uranium covariation—Applications to Mesozoic paleoceanography. Chemical Geology, 324–325: 46-58.
Tribovillard, N., 2020. Arsenic in marine sediments: how robust a redox proxy? Palaeogeography, Palaeoclimatology, Palaeoecology, 550: 109745.
Tyson, R., 1995. Sedimentary Organic Matter: Organic Facies and Palynofacies, London.
van de Velde, S.J., Reinhard, C.T., Ridgwell, A., Meysman, F.J.R., 2020. Bistability in the redox chemistry of sediments and oceans. Proceedings of the National Academy of Sciences, 117(52): 33043-33050.
van den Boogaart, G., Tolosana-Delgado, R., Bren, M., 2020. compositions: Compositional Data Analysis. R package version 2.0-0. https://CRAN.R-project.org/package=compositions.

ACCEPTED MANUSCRIPT

Van Mooy, B.A.S., Keil, R.G., Devol, A.H., 2002. Impact of suboxia on sinking particulate organic carbon: Enhanced carbon flux and preferential degradation of amino acids via denitrification. Geochimica et Cosmochimica Acta, 66(3): 457-465.
Veevers, J.J., Powell, C.M., 1987. Late Paleozoic glacial episodes in Gondwanaland reflected in transgressive-regressive depositional sequences in Euramerica. Geological Society of America Bulletin, 98(4): 475-487.
Vilà, M., Fernández, M., Jiménez-Munt, I., 2010. Radiogenic heat production variability of some common lithological groups and its significance to lithospheric thermal modeling. Tectonophysics, 490(3): 152-164.
Warr, L.N., 2000. The Variscan Orogeny: the welding of Pangaea. In: Woodcock, N.H., Strachan, R. (Ed.), Geological History of Britain and Ireland. Wiley-Blackwell, Hoboken, USA, pp. 271 - 294.
Warren, P.T. et al., 1984. Geology of the country around Rhyl and Denbigh Memoir for 1:50,000 geological sheets 95 and 107 and parts of sheets 94 and 106. Memoirs of the Geological Survey of Great Britain, England and Wales (Sheet - New Series). HMSO, London.
Waters, C.N., Davies, S.J., 2006. Carboniferous: extensional basins, advancing deltas and coal swamps. In: Brenchley, P.J. (Ed.), The geology of England and Wales. Geological Society of London, London, England, pp. 173 - 223.
Waters, C.N., Browne, M.A.E., Dean, M.T., Powell, J.H., 2007. Lithostratigraphical framework for Carboniferous successions of Great Britain (Onshore). British Geological Survey Research Report, RR/07/01.
Waters, C.N., Waters, R.A., Barclay, W.J., Davies, J.R., 2009. A lithostratigraphical framework for the Carboniferous successions of southern Great Britain (onshore). British Geological Survey Research Report, RR/09/01.
Waters, C.N. et al., 2011. A revised correlation of Carboniferous rocks in the British Isles, Geological Society of London Special Report, 26. Geological Society of London, Bath, UK, 186 pp.
Waters, C.N., Condon, D.J., 2012. Nature and timing of Late Mississippian to Mid-Pennsylvanian glacio-eustatic sea-level changes of the Pennine Basin, UK. Journal of the Geological Society, 169(1): 37-51.
Waters, C.N. et al., 2019. Lithological and chemostratigraphic discrimination of facies within the Bowland Shale Formation within the Craven and Edale basins, UK. Petroleum Geoscience.
Waters, C.N., Morton, A., Frei, D., 2020. Interplay of southern, western, and northern sources during deposition of North Wales Carboniferous sandstones, determined from heavy minerals, mineral chemistry, and detrital zircon ages. Geological Journal, n/a(n/a).
Wei, W., Algeo, T.J., 2019. Elemental proxies for paleosalinity analysis of ancient shales and mudrocks. Geochimica et Cosmochimica Acta.
Whitelaw, P. et al., 2019. Shale gas reserve evaluation by laboratory pyrolysis and gas holding capacity consistent with field data. Nature Communications, 10(1): 3659.
Wickham, H., 2009. ggplot2: Elegant Graphics for Data Analysis. Springer-Verlag New York.
Wickham, H., Francois, R., 2016. dplyr: A Grammar of Data Manipulation. R package version 0.5.0. https://CRAN.R-project.org/package=dplyr.
Wignall, P.B., 1994. Black shales. Clarendon Press ; Oxford University Press, Oxford; New York.
Williams, G.D., Eaton, G.P., 1993. Stratigraphic and structural analysis of the Late Palaeozoic–Mesozoic of NE Wales and Liverpool Bay: implications for hydrocarbon prospectivity. Journal of the Geological Society, 150(3): 489-499.
Worden, R.H. et al., 2020. Lower Cretaceous Rodby and Palaeocene Lista Shales: Characterisation and Comparison of Top-Seal Mudstones at Two Planned CCS Sites, Offshore UK. Minerals, 10(8): 691.
Zeileis, A., Grothendieck, G., 2005. zoo: S3 Infrastructure for Regular and Irregular Time Series. Journal of Statistical Software, 14(6): 1-27.

ACCEPTED MANUSCRIPT

Zijp, M., Nelskamp, S., Doornenbal, H., 2017. Resource estimation of shale gas and shale oil in Europe. Report T7b of the EUOGA study (EU Unconventional Oil and Gas Assessment) commissioned by European Commission Joint Research Centre to GEUS.

ACCEPTED MANUSCRIPT

Figure Captions

Fig. 1. Brigantian block-and-basin structures and key borehole and outcrop sections across central Britain, with emphasis on the vicinity of the Blacon Basin, after Andrews (2013); Fraser and Gawthorpe (1990); Fraser et al. (1990); Fraser and Gawthorpe (2003); Pharaoh et al. (2019a); Smith et al. (2005); Waters and Davies (2006); Waters et al. (2007); Waters et al. (2009); Waters et al. (2011); Waters et al. (2019); Waters et al. (2020).

Fig. 2. General stratigraphy, regional Arnsbergian lithofacies and selected well log data. (a) Generalized stratigraphy and (b) regional lithofacies from Waters et al. (2007), including absolute ages (from Waters and Condon, 2012 and Davydov et al., 2012) and the updated Early-Late Serpukhovian boundary (Cózar and Somerville, 2021). (c) The Bowland Shale Formation exhibits elevated total gamma ray (GR) and U (ppm) concentrations. (d) Correlation between wireline gamma versus synthetic gamma ray (estimated from measured U, Th and K contents; see Methods) verifies the alignment of reported corebox depths to the wireline data (see Figure 3). Ellesmere Port-1 is highlighted (53°17'43.3841", 02°54'21.13091"; 339629 mE 378016 mN, British National Grid).

Fig. 3. Key static borehole image (BHI) log and core observations used for the alignment of reported well and core depth. Depth alignment was achieved by matching the same linear features present in both datasets.

Fig. 4. Sedimentology and selected geochemistry through the late Arnsbergian-Chokerian Bowland Shale in Ellesmere Port-1 (core 2). See Figure 3 for key to sedimentary structures. Palynofacies data are from Hennissen et al. (this volume), using the fields of Tyson (1995). I = highly proximal shelf/basin, II = marginal dysoxic-anoxic basin, III = heterolithic (proximal) shelf, IVa = dysoxic-suboxic shelf edge, IVb = dysoxic-anoxic shelf edge, V = mud-dominated (distal) oxic shelf, VI = proximal suboxic-anoxic shelf, VII = distal dysoxic-anoxic shelf, VIII = distal dysoxic-oxic shelf, IX = distal suboxic-anoxic basin.

Fig. 5. Sedimentology and selected geochemistry through the late Kinderscoutian Bowland Shale in Ellesmere Port-1 (core 1). See Figure 3 for key to sedimentary structures. Palynofacies data are from Hennissen et al. (this volume), using the fields of Tyson (1995). I = highly proximal shelf/basin, II = marginal dysoxic-anoxic basin, III = heterolithic (proximal) shelf, IVa = dysoxic-suboxic shelf edge, IVb = dysoxic-anoxic shelf edge, V = mud-dominated (distal) oxic shelf, VI = proximal suboxic-anoxic shelf, VII = distal dysoxic-anoxic shelf, VIII = distal dysoxic-oxic shelf, IX = distal suboxic-anoxic basin.

Fig. 6. Clay, carbonate and quartz bulk compositional ternary plot, estimated using scaled core scan XRF count data; 2Al, 0.1Ca and 10Zr, respectively. See text for discussion.

Fig. 7. Excess silica biplots, after Emmings et al. (2020b). Regression lines for the Ellesmere Port-1 data (red line, with 95% confidence interval) and Emmings et al. (2020a) are also plotted. The excess Si field delineates siliceous mudstones. The field is calibrated for Bowland Shale mudstones and compositionally immature siltstones and is not necessarily valid for other sedimentary rocks. Figure 6 for key to facies.

Fig. 8. Major and trace element enrichment factors for chemofacies A-G, normalized to the chemofacies F-G (oxic-suboxic) mean. Red lines for the enrichment factor plots are mean curves. Bottom right: $\delta^{34}S_{bulk}$, $\delta^{13}C_{org}$ and C/N histograms and density curves for chemofacies A-G.

ACCEPTED MANUSCRIPT

Fig. 9. Geochemical proxies for bottom water salinity and redox. (a) S/TOC (Berner and Raiswell, 1984) and Sr/Ba (Wei and Algeo, 2019) palaeosalinity proxies. Fields are bounded by the thresholds for salinity as defined in Wei and Algeo (2019), favouring the more widely established S/TOC proxy. Conflict zones could indicate decoupling between the S/TOC and/or Sr/Ba proxies, likely due to diagenetic effects. Circled data points exhibit inorganic C > 0.3 wt. %, a local threshold for Sr-bound and/or Ba-associated carbonate. In these cases, the Sr/Ba palaeosalinity proxy is invalid (Wei and Algeo, 2019). (b) Mo versus U enrichment factors (EFs) (Algeo and Tribovillard, 2009; Tribovillard et al., 2012) suggest fluctuation between oxygenated and weakly to moderately anoxic, intermittently sulphidic particulate shuttle conditions. (c) Mo versus TOC suggests deposition under weakly restricted bottom water conditions (Algeo and Lyons, 2006). See methods for calculation of enrichment factors and derivation of original TOC (TOC_o). (d-e) Interpreted redox and salinity response to fourth-order sea level fluctuation, assuming productivity-driven anoxia in a weakly restricted basin (*sensu.* Emmings et al., 2020c). The fourth-order cyclicity is partially overprinted by progradation of the Cefyn-y-fedw delta system. AMO = anaerobic oxidation of methane.

Fig. 10. The results of three K-nearest neighbours (kNN) predictive chemofacies models. (a) Chemofacies were derived from PCA and HCA of selected XRF core scan elements, simplified (aggregated), and matched to the nearest wireline datum. The models were trained and deployed by matching the XRF-derived chemofacies to selected wireline logs. kNN (1-3) represent different approaches (see Methods). (b) The trained models were deployed on the observed Bowland Shale section at Ellesmere Port-1 (1443 to 1767 m below surface) (kNN method 2 is displayed). Prominent sand packages likely correspond to lower, middle and upper extensions of the Cefn-y-fedw sandstone (Waters et al., 2020) coincident with three periods of regional channel incision (Waters and Condon, 2012). Biostratigraphic ammonoid zones observed in core (bold), other inferred major flooding events and biozones (italicized, from Davies et al., 2011) and interpreted substages and extrapolated ages (Waters and Condon, 2012) are also indicated.

Fig. 11. Summary of interpreted Namurian sedimentary architecture in the Blacon Basin, with major flooding events of Davies et al. (2011) and general stratigraphy after Magraw and Ramsbottom (1957), Davies et al. (2004), Smith et al. (2005), Waters et al. (2009), Andrews (2013) and Waters et al. (2020). The shelf-edge delta wedge of the Late Pleistocene Po River (Adriatic Sea, offshore central Italy) may represent a partial (albeit short-lived) modern analogue (Patruno and Helland-Hansen, 2018; Pellegrini et al., 2017). Gamma-ray well logs for Croxteth-1, Ellesmere Port-1 (this study), Blacon East-1 and Milton Green-1 are shown for reference. See Figure 1 for line of section.

Fig. 12. Comparison of radiogenic heat productivities (RHPs) and U, Th and K concentrations for a range of rock types. (a) Calculated RHPs through the Bowland Shale based on the spectral gamma well log data, superimposed with the machine predictions. (b-c) RHPs and U, Th and K concentrations for limestone, claystone, calcareous mudstone, and siltstone-sandstone facies in the Bowland Shale in Ellesmere Port-1, based on spectral gamma and discrete XRF analysis (the latter indicated by *). The UK RHP sedimentary mean (Busby and Terrington, 2017; Rollin, 2002) and RHPs for the Bowland Shale in the Craven Basin (Emmings et al., 2020c; Newport, 2019), the Kimmeridge Clay (Yorkshire, unpublished), Holywell Shale (Newport et al., 2016) and italicized baseline data (Vilà et al., 2010) are also shown.

ACCEPTED MANUSCRIPT

Fig. 13. Measured versus modelled temperature gradients through the Bowland Shale Formation in Ellesmere Port-1. It should be noted the borehole temperatures are unlikely to represent true, equilibrated values and therefore likely represent minimum estimates.

ACCEPTED MANUSCRIPT

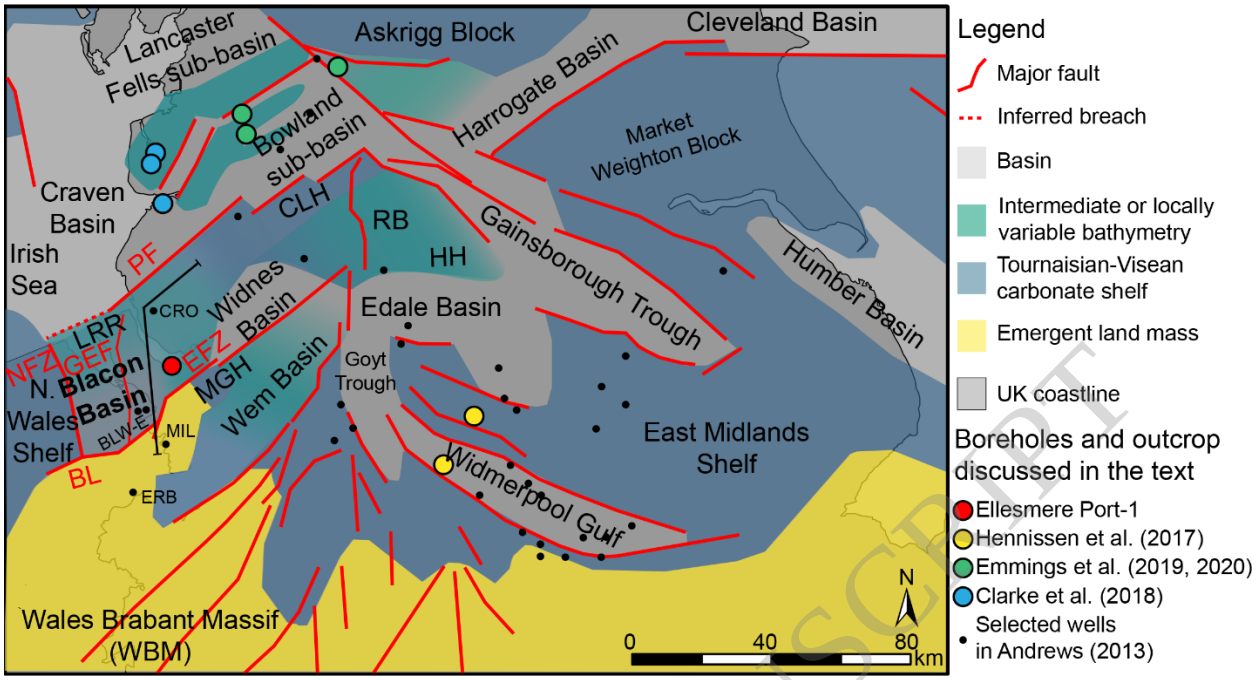

ACCEPTED MANUSCRIPT

Figure 1

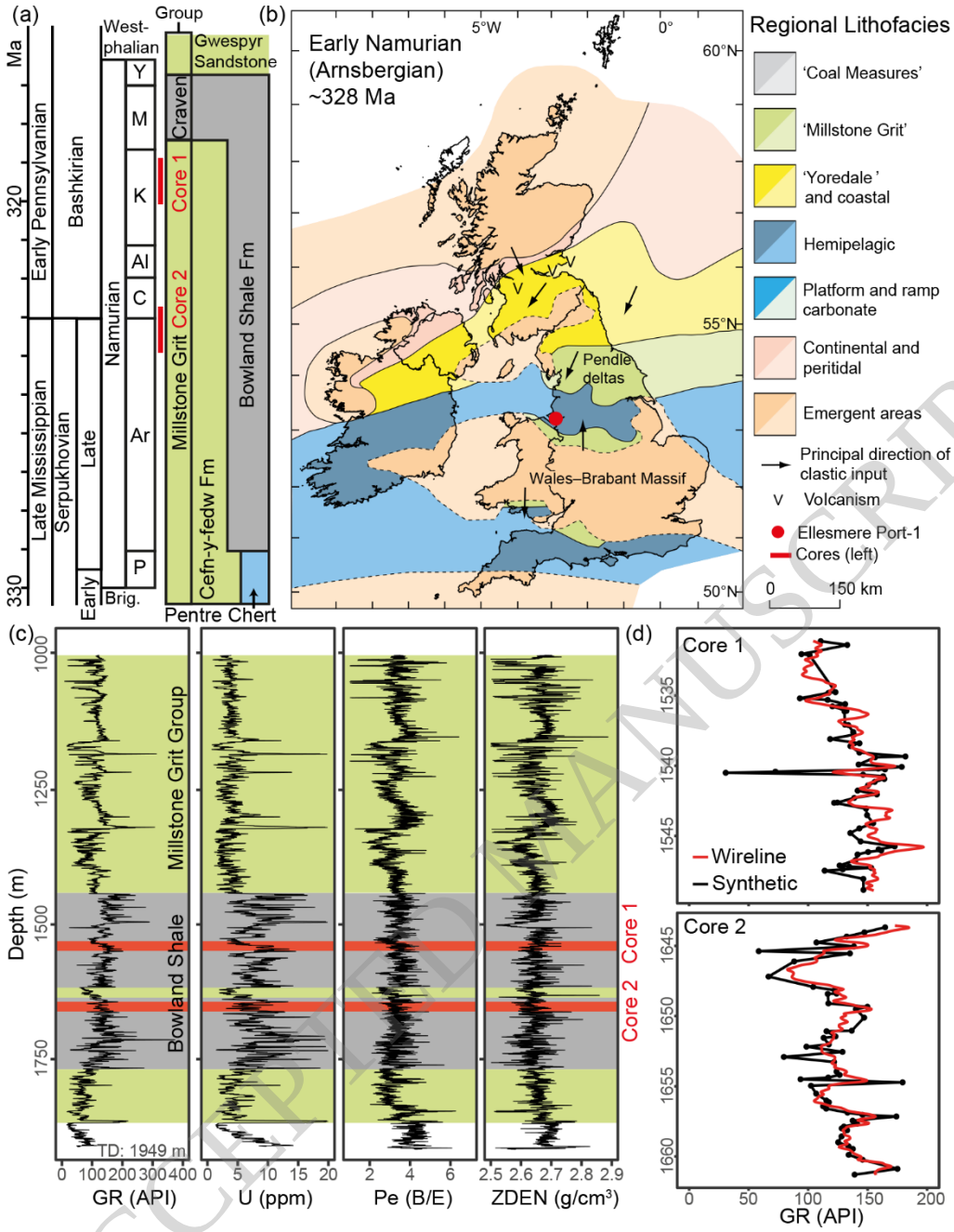

ACCEPTED MANUSCRIPT

Figure 2

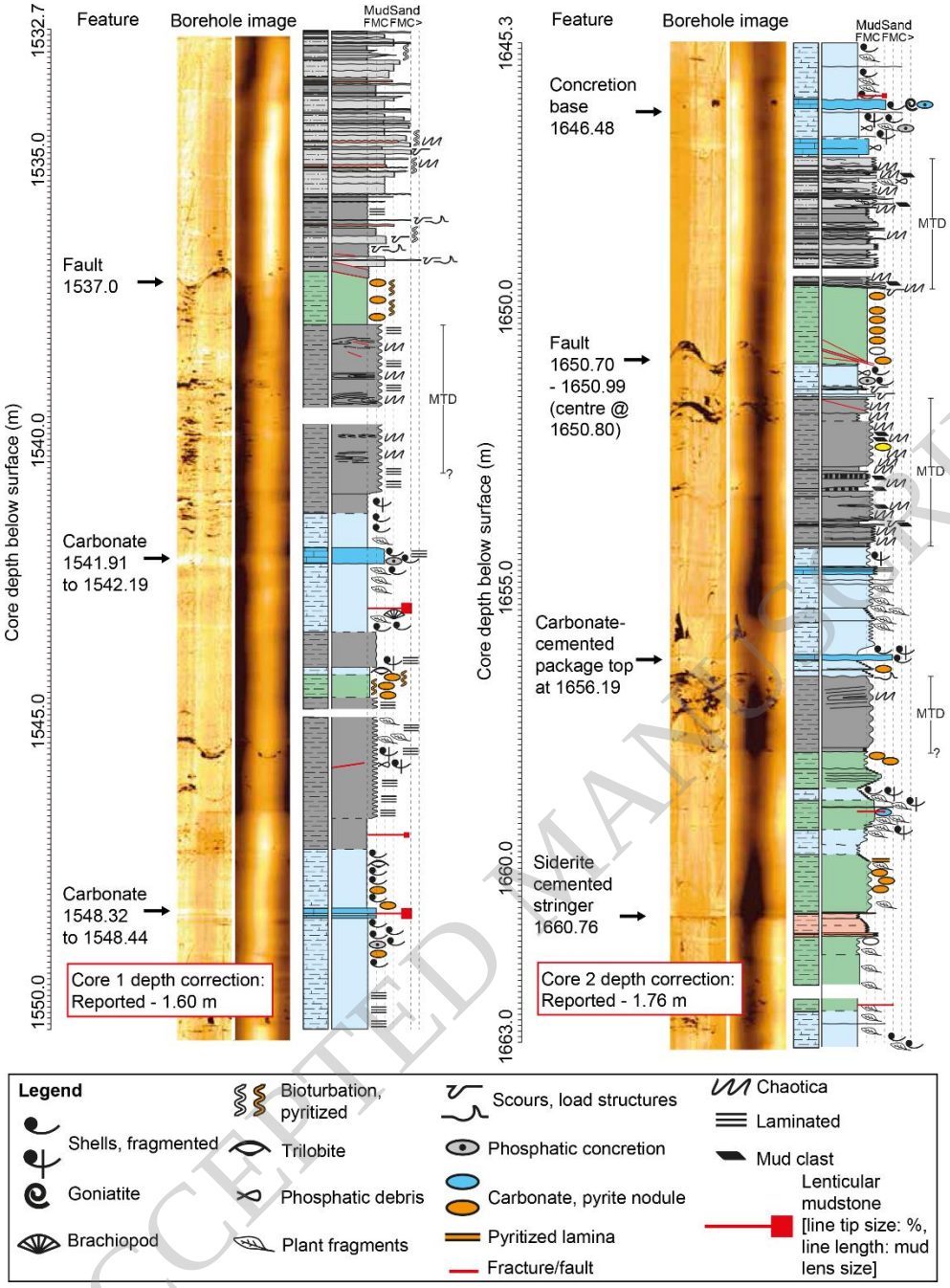

ACCEPTED MANUSCRIPT

Figure 3

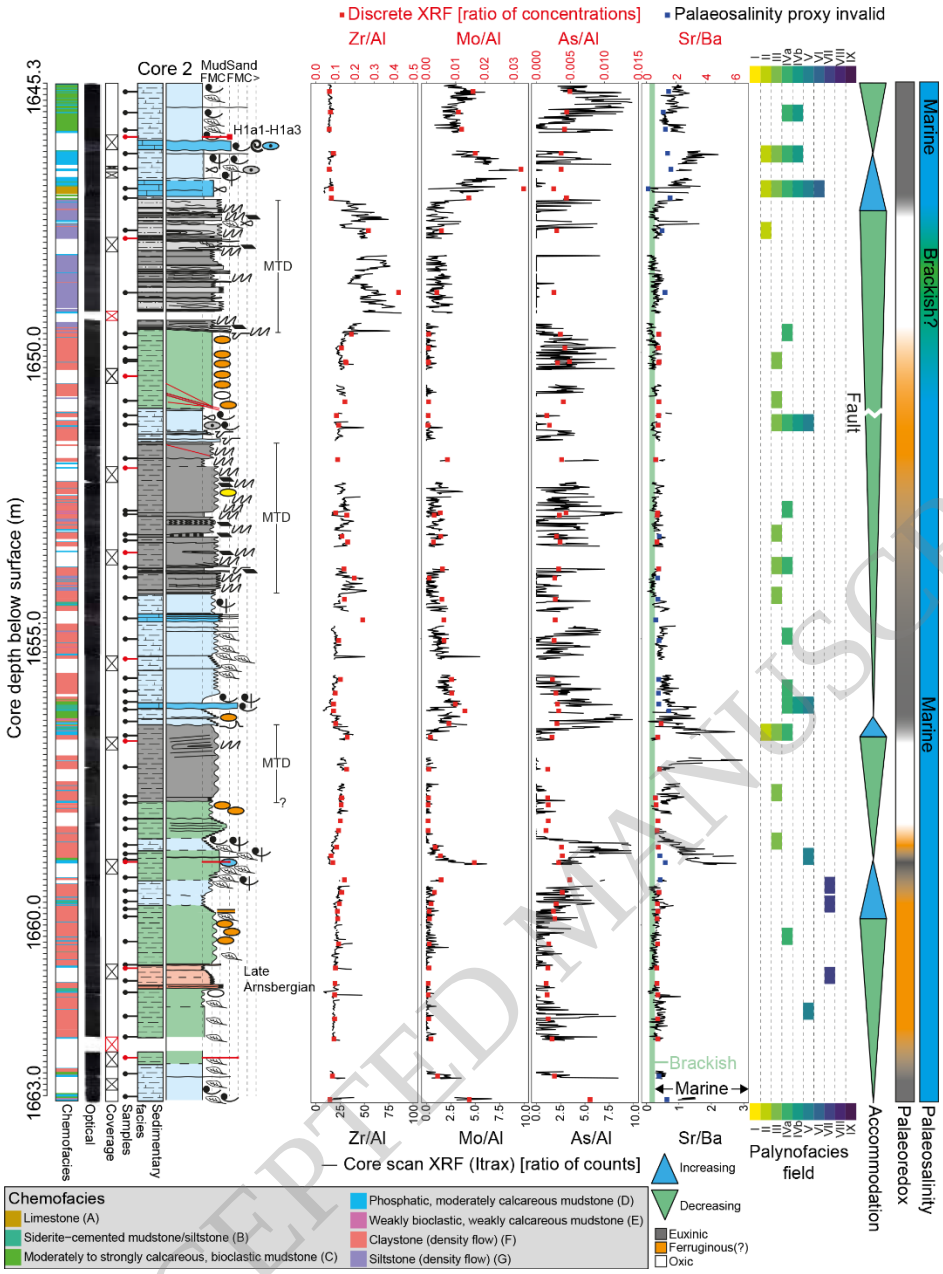

ACCEPTED MANUSCRIPT

Figure 4

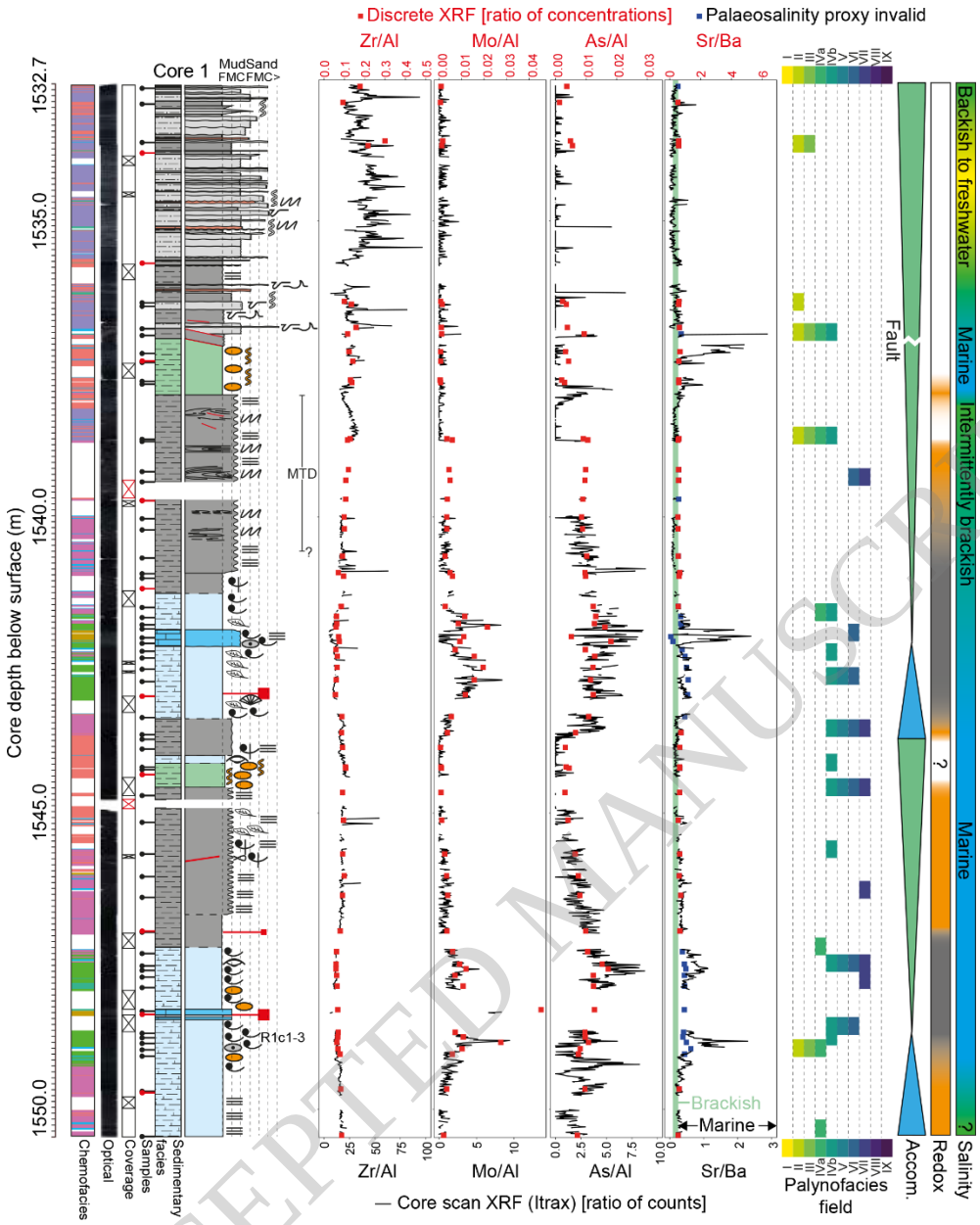

ACCEPTED MANUSCRIPT

Figure 5

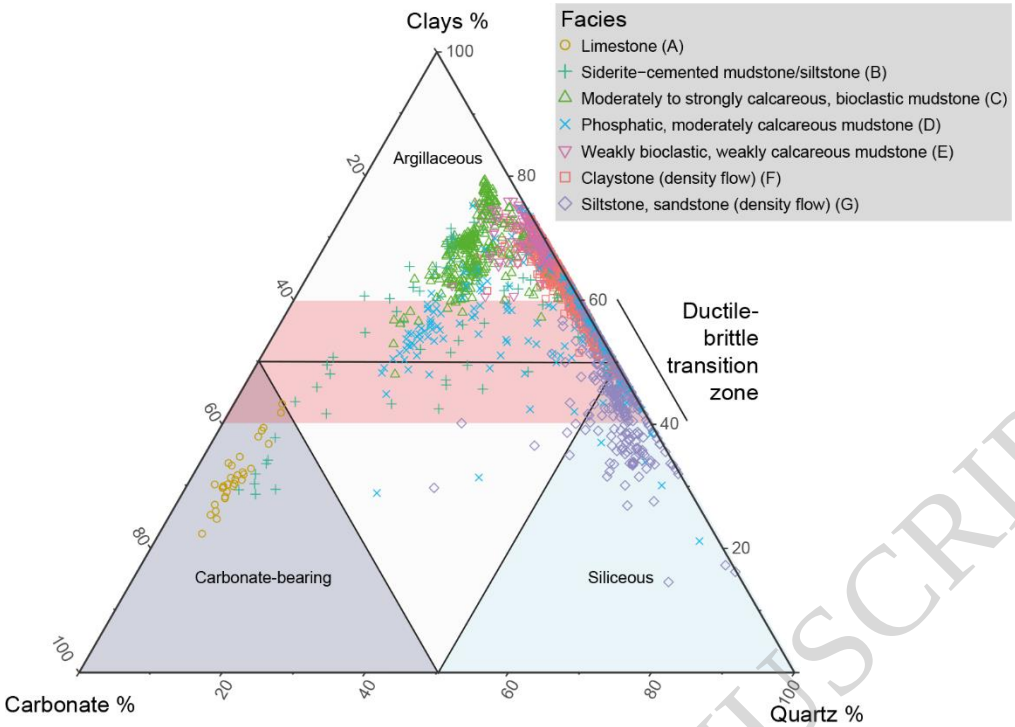

ACCEPTED MANUSCRIPT

Figure 6

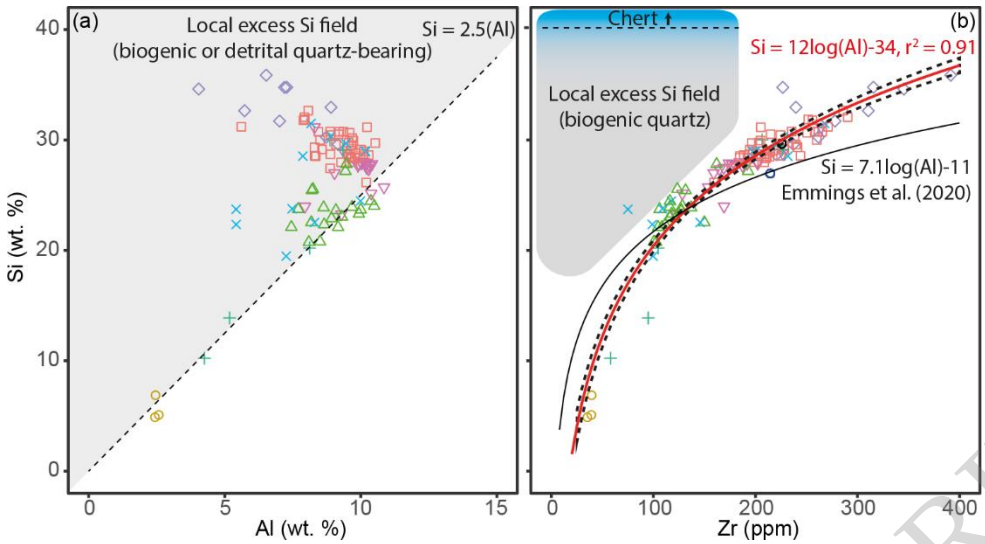

ACCEPTED MANUSCRIPT

Figure 7

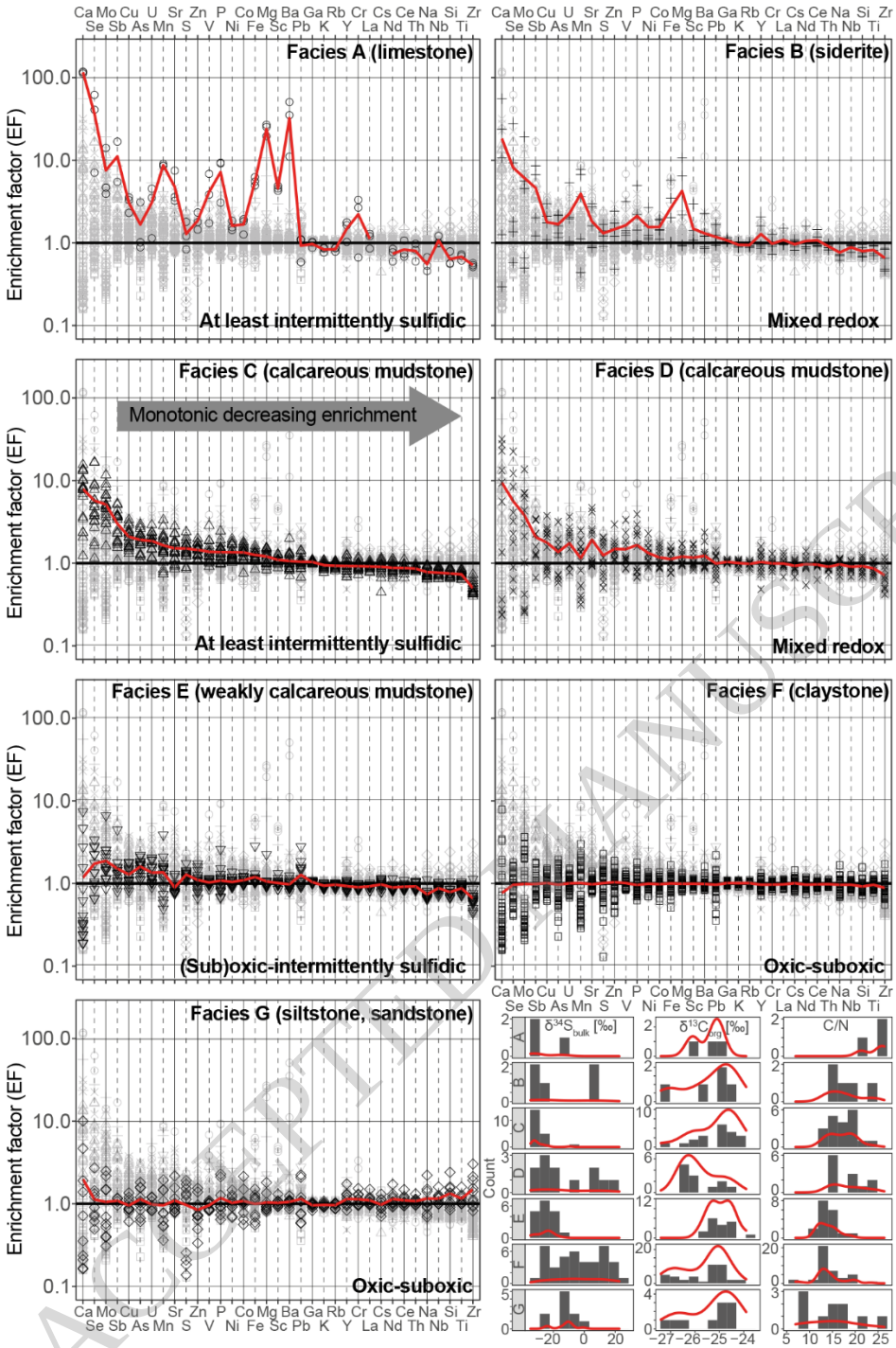

ACCEPTED MANUSCRIPT

Figure 8

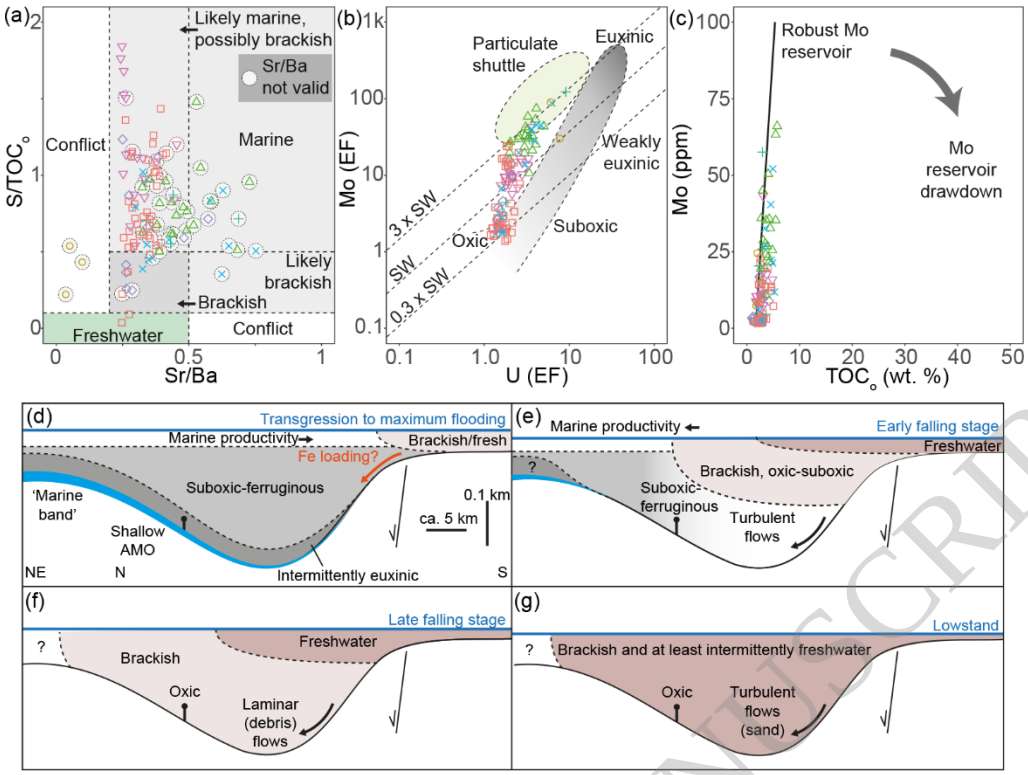

ACCEPTED MANUSCRIPT

Figure 9

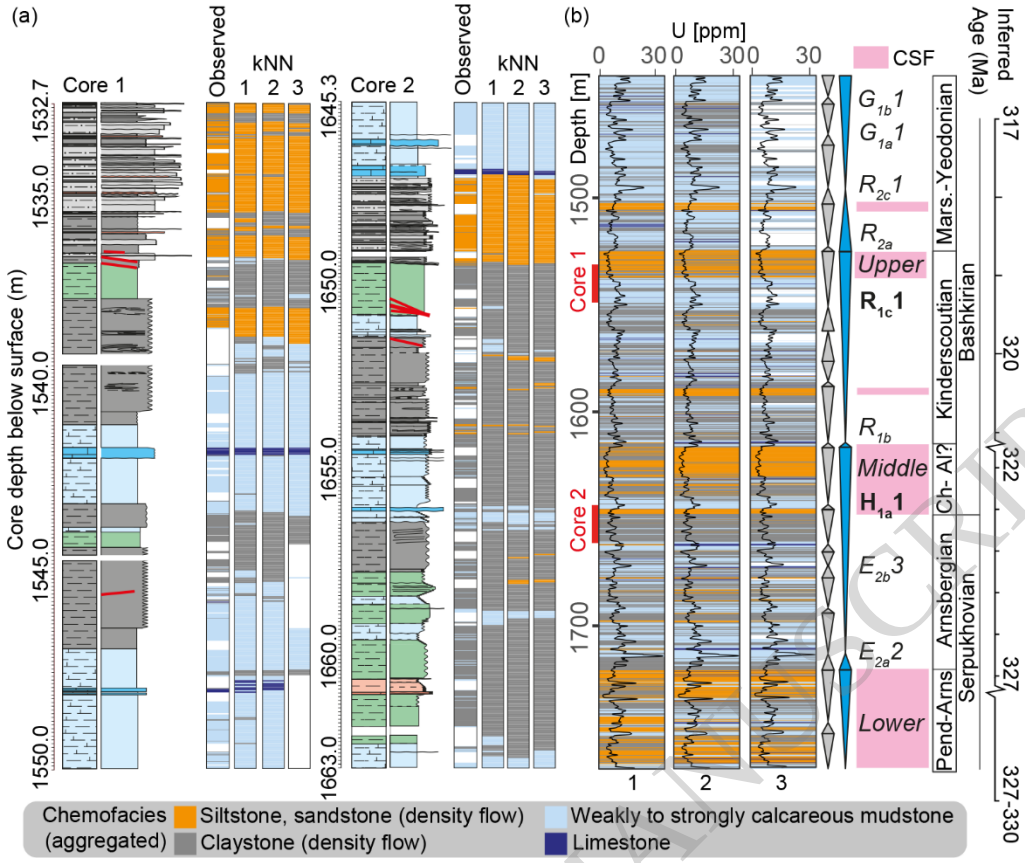

ACCEPTED MANUSCRIPT

Figure 10

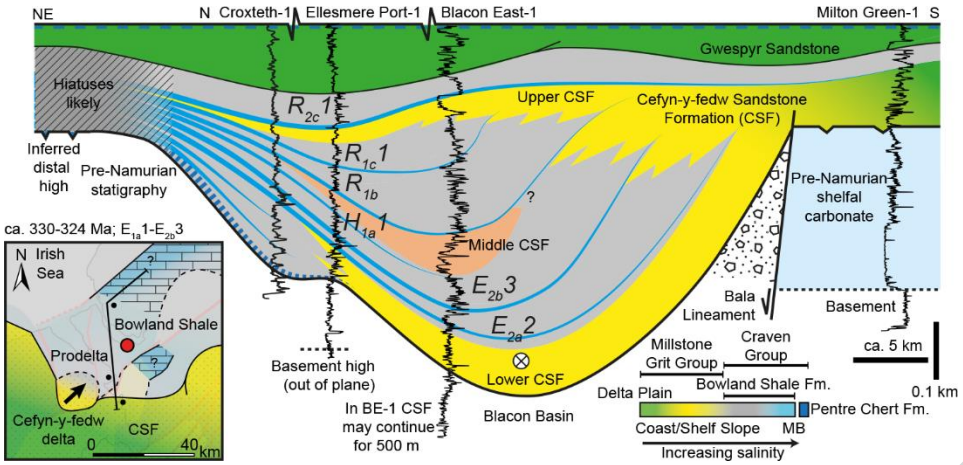

Figure 11

ACCEPTED MANUSCRIPT

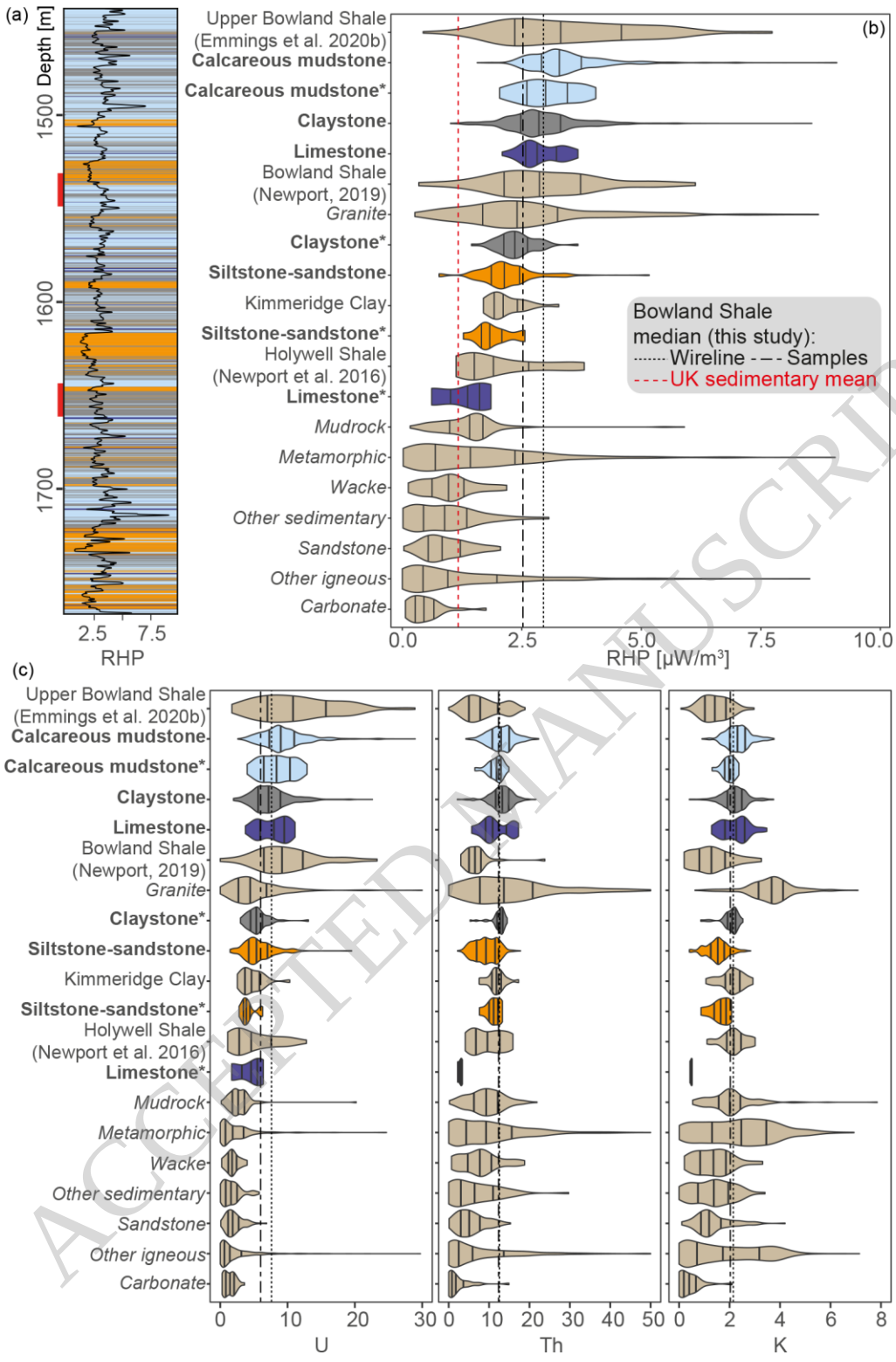

ACCEPTED MANUSCRIPT

Figure 12

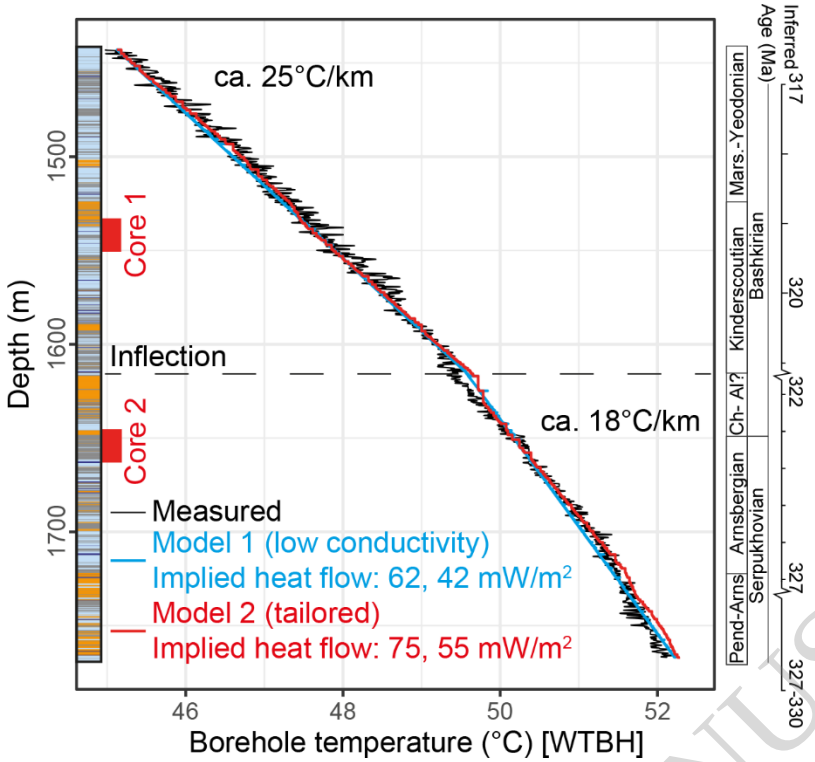

ACCEPTED MANUSCRIPT

Figure 13